Chemical Engineering Research and Design 206 (2024) 469–488

Contents lists available at ScienceDirect

Chemical Engineering Research and Design

journal homepage: www.elsevier.com/locate/cherd

Feedback control of an experimental electrically-heated steam methane reformer

Berkay Çıtmacı [a], Dominic Peters [a], Xiaodong Cui [a], Fahim Abdullah [a], Ahmed Almunaifi [a], Parth Chheda [a], Carlos G. Morales-Guio [a], Panagiotis D. Christofides [a,b,*]

[a] Department of Chemical and Biomolecular Engineering, University of California, Los Angeles, CA, 90095-1592, USA
[b] Department of Electrical and Computer Engineering, University of California, Los Angeles, CA 90095-1592, USA

ARTICLE INFO

Keywords:
Steam methane reforming
Experimental data modeling
Digitalization
Model predictive control (MPC)
State observers
Process control

ABSTRACT

Steam methane reforming (SMR) is the most common industrial process to produce hydrogen (H_2) from methane and water vapor. The SMR reactions are overall highly endothermic and traditionally, fossil fuels are burned to provide the necessary heat of reaction. However, it was found that electrifying the tubular SMR reactors using renewable electrons instead of conventional heating gives the opportunity of producing H_2 with lower carbon emissions, lower reactor volumes, and higher carbon conversion. While current studies in this new technology focus on improving the catalysts or heating sources, a more efficient process control scheme can also significantly contribute to the understanding of potential challenges and opportunities of combining renewables and natural gas in the production of H_2 at industrial scales. In order to further develop the electrically-heated SMR process and the associated control strategies, we have constructed an experimental Joule-heated SMR system at UCLA. The system contains a tubular reactor with a washcoated Ni/ZrO_2 catalyst, two thermocouples connected to the top and bottom of the reactor, a power supply for providing electrical heating, and an on-line gas chromatograph (GC) for measuring outlet gas concentrations. The synthesis procedure of the catalyst, SMR data collection, and thermal considerations for catalyst degradation are described in this paper and are all accounted for experimentally when using a proportional integral (PI) controller to gradually increase the reactor temperature without harming the catalyst. Advanced control strategies, such as model predictive control (MPC), require a process model that uses measurement feedback to make predictions of the process time-evolution in order to optimize the control actions in real-time. We have previously developed a lumped-parameter modeling strategy for the SMR process. The MPC objective is to control the H_2 production rate by manipulating the current flowing through the outer reactor shell. However, to use this model in an MPC, feedback values for all state variables should be provided by the sensors. In our experimental system, the on-line GC only gives discrete measurements with a long sampling period. To this end, the process model is incorporated into an extended Luenberger observer (ELO) that uses the reactor temperature and GC measurements to provide estimates of all the variables needed by the MPC. The ELO-based MPC system is then experimentally implemented on the process and it is demonstrated to be more efficient in terms of speed of the closed-loop response than the PI controller using delayed, measurement feedback by the GC.

1. Introduction

Steam methane reforming (SMR) is an industrial process that converts methane and steam into hydrogen and carbon dioxide through the chemical reactions shown below:

$$\text{Steam methane reforming}: CH_4 + H_2O \rightleftharpoons 3H_2 + CO, \quad \Delta H_{298} = 206.1 \text{ kJ mol}^{-1} \tag{1a}$$

$$\text{Water gas shift}: CO + H_2O \rightleftharpoons CO_2 + H_2, \quad \Delta H_{298} = -41.15 \text{ kJ mol}^{-1} \tag{1b}$$

The highly endothermic reforming reaction and the slightly exothermic water gas shift reaction occur in series and parallel. Traditionally, these reactions take place in a packed-bed reactor placed in a fired furnace that burns fossil fuels. About thirty years ago, Spagnolo et al. (1992) introduced the idea of an electrically-heated SMR. Recently, Wismann et al. (2019) conducted a detailed experimental and modeling study to investigate the process and its potential to replace the conventional furnace heating with electrical heating, and reported that electrical heating leads to lower reactor volumes, causes less waste-heat, and

* Corresponding author at: Department of Chemical and Biomolecular Engineering, University of California, Los Angeles, CA, 90095-1592, USA.
E-mail addresses: moralesguio@ucla.edu (C.G. Morales-Guio), pdc@seas.ucla.edu (P.D. Christofides).

https://doi.org/10.1016/j.cherd.2024.05.021
Received 3 May 2024; Received in revised form 13 May 2024; Accepted 15 May 2024
Available online 18 May 2024

reduces CO_2 emissions if renewable electricity is used. Also, a Joule-heating energy source provides radially uniform heat distribution, causing the gas mixture to be at close-to-equilibrium conditions through a washcoated catalyst. The resistance-heated SMR process is further expected to reduce carbon formation, thus increasing the carbon conversion to hydrogen. The adoption of a Joule-heating process has also a potential to reduce global CO_2 emissions (Wismann et al., 2019). While the transition to a resistance-heated SMR process is still in its infancy, the current bench scale efforts can offer strategies and explorations to ease the adoption process.

With respect to previous work on this topic, Wismann et al. (2021) experimentally examined process dynamics including the effect of the heating rate on the start-up phase of the reactor, cyclic heating, and carbon formation at transient and steady-state conditions. Almind et al. (2020) focused on improving coil geometry and magnetic field frequency of an induction-heating setup and showed that thermal efficiency can be improved up to 12% compared to their initial bench scale coil geometry. In Zheng et al. (2023), a Rh/Al_2O_3 catalyst coated with silicon carbide (SiC) layer was washcoated across the reactor tube. The SiC layer increased the resistance for heating, and experimental results were reported to reach full conversion of methane. To explore further use of ohmic heating in reforming processes, From et al. (2024) moved to a pilot plant phase to test a process that uses biogas to produce syngas.

In addition to endeavors that improve SMR reactor heat flux, process design, and catalysts, one key component that can optimize the electrified SMR process is efficient feedback control to optimize the speed of transition to different set-points. The SMR reaction, especially in a fired-heater where the temperature gradients vary significantly in both axial and radial directions, is very complicated and thus very difficult to model. The reactions occur in a tubular reactor, and considering the variation in heat, mass, and momentum transfer coupled with reaction kinetics and temperature- or pressure-dependent variables like volumetric flowrates, such modeling requires solving partial differential equation (PDE) models. Consequently, commercial PDE solvers (e.g., COMSOL, Ansys Fluent) are widely used to model the SMR process. Specifically, Wu et al. (2017) simulated the reforming process in a furnace using a detailed computational fluid dynamics (CFD) model, linearized the model using the simulation data, and solved a quadratic programming problem to implement a model predictive control (MPC) scheme to the CFD model. More recently, Ting et al. (2023) built an Aspen Dynamic model to generate process data and carried out state-space identification to employ an MPC scheme in a computational study. However, efforts to experimentally implement and evaluate efficient real-time SMR process control are limited. In particular, and to the best of our knowledge, the advanced control of a Joule-heated SMR system with a washcoated catalyst has not been studied.

Our previous work has demonstrated successful single-input-single-output, multi-input-multi-output, and predictive control of experimental electrochemical reactors (Çıtmacı et al., 2022a, 2023; Luo et al., 2023). Furthermore, Çıtmacı et al. (2022b) presented how experimental setups can be digitalized using appropriate software and tools. Utilizing our experience in digitalization, modeling, and control, in Çıtmacı et al. (2024), we proposed a lumped parameter modeling approach that can be rapidly optimized in real-time. For this lumped parameter model, mass and energy balance equations were derived for varying parameters, and in a detailed computational study, this model was used in an MPC to demonstrate that the H_2 concentration can be effectively driven to the desired H_2 set-point. However, this computational work did not account for the experimental challenges, such as unmeasured variables like the molar or volumetric flowrates of steam. Thus, in a recent work (Cui et al., 2024), we developed a model predictive control method accounting for the issues encountered in the experimental setup, and in the present work, the MPC scheme proposed in Cui et al. (2024) and Çıtmacı et al. (2024) is implemented experimentally. Specifically, an extended Luenberger observer (ELO) is used to account for the missing feedback parameters and the ELO-based MPC closed-loop performance is compared to the one of a PI control system.

2. Preliminaries

2.1. Nomenclature

Definitions of variables used in the modeling of the reactor:

- A_j: Pre-exponential factor for adsorption constant K_j of gas species j [mol $(m^2\ s)^{-1}$]
- A_i: Pre-exponential factor for rate coefficient k_i for reaction i [mol $Pa^{0.5}$ $(kg-cat\ s)^{-1}$ for i = 1 (SMR reaction), mol Pa $(kg-cat\ s)^{-1}$ for i = 2 (WGS reaction)]
- C_i: Concentration of species i [mol m^{-3}]
- C_{p_i}: Specific heat capacity of gas species i [J $(mol\ K)^{-1}$]
- F: Total molar flow of gases [mol s^{-1}]
- F_i: Total molar flow of gases of gas species i [mol s^{-1}]
- K_j: Adsorption constant of gas species j [m^3 mol^{-1}]
- k_i: Reaction rate constant of reaction j [mol $Pa^{0.5}$ $(kg-cat\ s)^{-1}$ for i = 1 (SMR reaction), mol Pa $(kg-cat\ s)^{-1}$ for i = 2 (WGS reaction)]
- P_i: Partial pressure of gas species i [Pa]
- q: Outlet volumetric flowrate [m^3 s^{-1}]
- q_i: Outlet volumetric flowrate of gas species i [m^3 s^{-1}]
- r_i: Rate of reaction for reaction i [mol $(m^3\ s)^{-1}$]
- R: Universal gas constant [J $(mol\ K)^{-1}$]
- $\tilde{R}$: Cell resistance [Ω]
- T: Reactor temperature [K]
- T_{p_i}: Temperature of inlet gas species i [K]
- T_s: Temperature of the surroundings [K]
- UA: Overall heat transfer coefficient times the heat transfer area [J $(s\ K)^{-1}$]
- V: Reactor volume [m^3]
- Q: Power [W]
- W: Catalyst weight [kg]
- ΔH_r: Heat of reaction [J mol^{-1}]
- ΔH_{r_i}: Heat of reaction i [J mol^{-1}]
- $\dot{m}_{p_i}$: Mass flow rate of gas species i [kg s^{-1}]
- ρ_i: Density of the gas species i in the reactor [kg m^{-3}]

2.2. Experimental system and digitalization

At UCLA, we have established an experimental steam methane reforming setup to investigate the efficiencies of various promising and novel hydrogen production methods. Transforming conventional-heating reformers into Joule-heating reformers is relatively straightforward, only requiring a modification in the heating source, and this work begins an investigation into the efficiencies, modeling, and control strategies of these electrically-heated experimental reforming systems. In order to minimize axial pressure drop, a Ni/ZrO_2 washcoat was deposited on the inner wall of the tubular reactor. The experimental and digitalization overview of the reactor are shown in Fig. 1.

The experimental setup involves monitoring various parameters such as temperature, pressure, and current. Multiple sensors including thermocouples and pressure transducers are utilized for measurement. All sensors and actuators are connected to a Laboratory Virtual Instrument Engineering Workbench (LabVIEW) interface, a graphical coding platform that is very convenient for connecting data acquisition and actuation systems. LabVIEW has built-in drivers for various process equipment components, and many companies develop external drivers that can be incorporated into LabVIEW for digitalizing their own equipment. Three thermocouples (Omega K-type) are positioned throughout the system: one on the bottom of the exterior reactor wall (13.5 cm from the reactor outlet), the second one on the top of the exterior reactor wall (34.5 cm from the reactor outlet), and the third

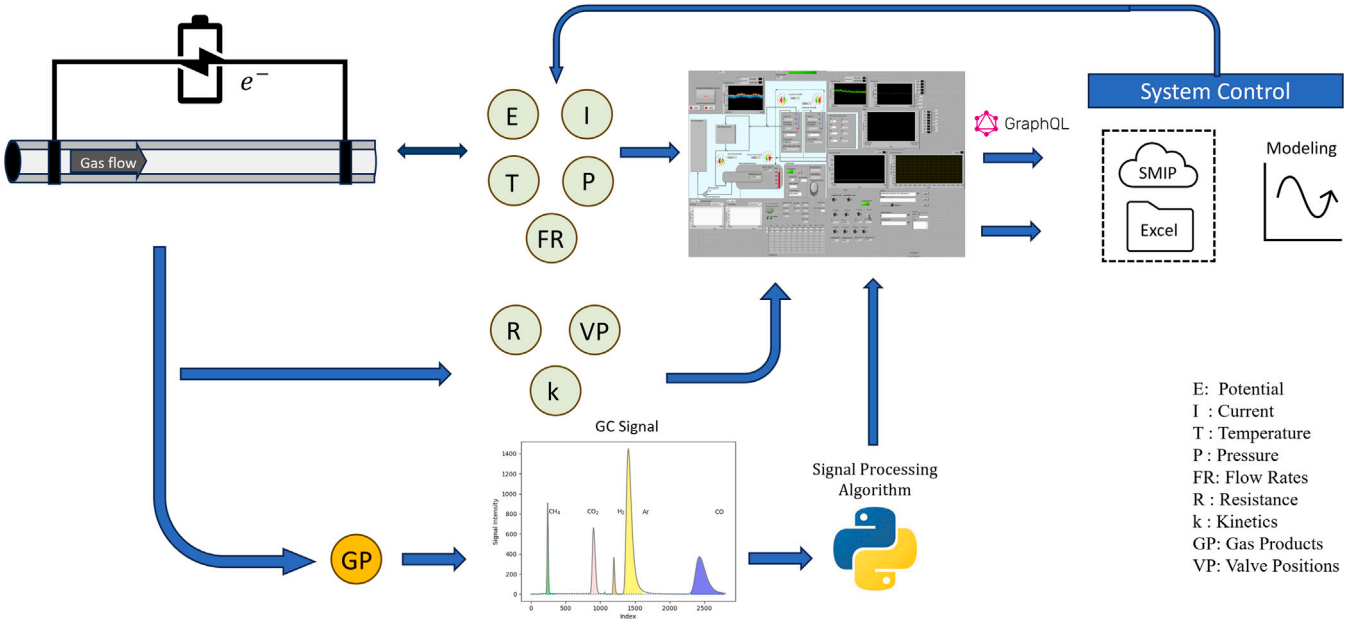

Fig. 1. Process flow diagram for experimental Joule-heating steam methane reforming process.

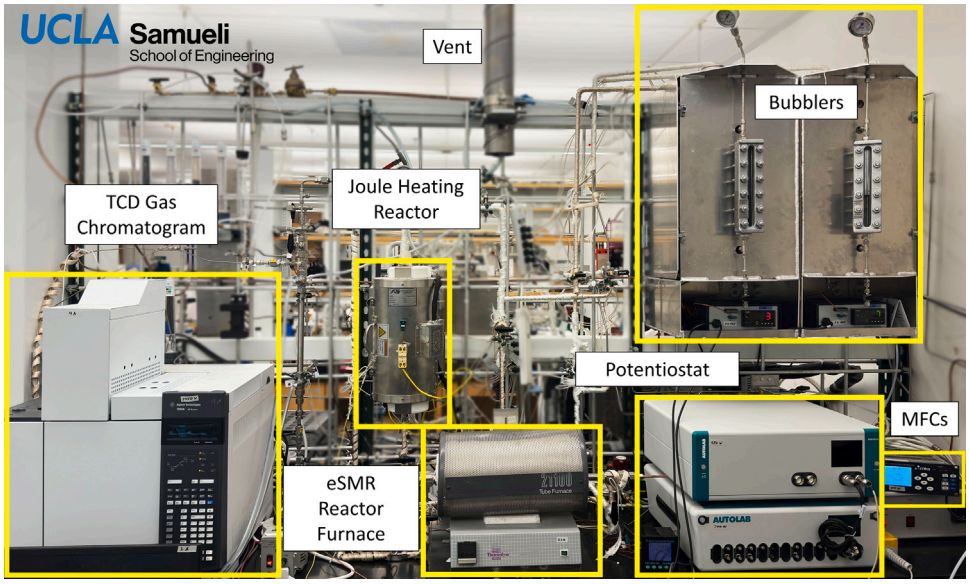

Fig. 2. Picture of experimental setup.

on the upstream gas flow pipe that is heated to 150 °C to prevent steam condensation. A single pressure transducer (Omega PX359 - 1KAI) measures reactor pressure and may be maintained at a constant value using a back pressure regulator (Equilibar). Thermocouples, back pressure regulators, and pressure transducers are digitized through a National Instruments Compact Rio, an industrial grade, reconfigurable data acquisition system. The experimental setup is shown in Fig. 2.

In addition to the sensors and actuators in connection to the Compact Rio, a Chroma programmable DC power supply connects to LabVIEW as well. The reactor-power supply setup controls the current supplied to the reactor and measures the corresponding potential in a closed-loop configuration. The power supply is connected to the LabVIEW interface through external Chroma drivers. The energy given to the experimental setup is shown in Eq. (2a) below, where Q is the rate of heat supply and the average resistance value ($\bar{R}$) can be found as the ratio of potential, E, to current values, I using the entire time series data, as shown in Eq. (2b) below:

$$Q = I^2 \bar{R} \tag{2a}$$

$$\bar{R} = \frac{E}{I} \tag{2b}$$

The tubular reactor is the central component of the Joule-heated SMR setup. Constructed with a 72.8% Fe, 22% Cr, 5% Al, 0.1% Y, and %0.1 Zr alloy procured from Goodfellow Corp., it features dimensions of 500 mm length, 6 mm outer diameter, and 5.4 mm inner diameter (Çıtmacı et al., 2024). The reactor tube is enveloped by fiberglass-based insulation to minimize heat losses, while an additional insulation furnace, equipped with ceramic foam material, provides further heat retention. In this study, the joule-heated system sits inside an Ascon Technologic R38S electric furnace that can be used to provide heat similar to a conventional fired SMR process, but that is turned off in all the joule-heating experiments presented here, unless otherwise indicated.

Gas phase products are analyzed in real-time using an Agilent Technologies 7890B gas chromatograph equipped with a thermal conductivity detector (TCD). The gas mixture undergoes condensation to remove water vapor before entering the GC, where components including H_2, CO_2, CO, and unreacted CH_4 are quantified. Each analysis cycle lasts 15 min, followed by a 3-min cool-down period. Consequently, the GC can process one gas sample every 18 min. Automated GC analysis is triggered by an external Python code, with results automatically processed post-measurement to determine peak areas and compare them to calibrated values for each gas species. The signal processing algorithm used is discussed in detail in Çıtmacı et al. (2022b). The gas chromatograph does not directly measure concentration or molar flowrate, rather it measures the molar percentage of the gases in the injection volume. This is based on the initial calibration of the GC, where various known molar ratios of gases were sent to the GC, and corresponding peak areas were recorded. After multiple gas mixtures were calibrated, the peak areas and corresponding percentages were fitted to power functions, which are used in real-time for quantifying the gas phase products. The sum of all percentages must be equal to 100% for an accurate gas quantification.

The inlet flowrates provided to the system are adjusted by a mass flow-meter (MKS). The flow-meter unit is standard cubic centimeters per minute (sccm). Trace amounts of Ar gas is flown through the system during each experiment to track molar flowrate changes in the outlet gas mixture. Argon is a noble, inert gas that does not react with other gases during the SMR process. As a result, the inlet molar Ar flowrate will be equal to outlet molar Ar flowrate, except for the very brief period of reactor startup.

The mass flow-meter is calibrated before each experiment. A specific flowrate input for each inlet gas (e.g., CH_4, H_2, Ar) that will be used for the experiment is entered on the flow-meter input panel and the corresponding GC injection output (in %) is recorded. First, the percentage of Ar that comes from the automated GC code is accepted to be the Ar basis. The sum of inlet gases (in sccm) shown on the mass flow controller is accepted to be the flow basis ($flow_{basis}$), and this is a constant value throughout the experiment for a constant inlet flowrate experiment. With each GC measurement, the Ar basis is divided by the Ar percentage in the injection volume to estimate the flow factor ($flow_{factor}$). In each GC measurement, the Ar peak area (and thus percentage) might change, however, since the molar flowrate of Ar will not change, Eq. (3) below can be used to estimate the molar flowrate of each species:

$$F_i\ [\text{sccm}] = \frac{GC_i[\%]}{100} \times flow_{basis}\ [\text{sccm}] \times flow_{factor}, \quad i = \text{CH}_4, \text{CO}, \text{H}_2, \text{CO}_2, \text{Ar} \tag{3}$$

The flow factor is accounting for the change in the entire molar flowrate compared to the initial total flowrate by adjusting the molar fraction of the constant flowrate of Ar in the injection volume. The conversion for molar flowrate from mol/s to sccm is shown in Eq. (4) below:

$$F\left[\frac{\text{cm}^3}{\text{min}}\right] = 1000\left[\frac{\text{cm}^3}{\text{L}}\right] \times 22.4\left[\frac{\text{L}}{\text{mol}}\right] \times F\left[\frac{\text{mol}}{\text{s}}\right] \times 60\left[\frac{\text{s}}{\text{min}}\right] \tag{4}$$

The SMR system is equipped with two steam boxes that can supply steady inlet streams of water vapor to the electrically heated tubular reactor; however, only one unit is needed for the investigated setup. Each steam box houses a bubbler encased within fiberglass thermal insulation. Using a K-type thermocouple, an Arcon temperature actuator, and electrical heating tape, the bubbler is set to a desired steam-to-carbon (s/c) ratio via temperature control. The Antoine equation, shown in Eq. (5) below, estimates the vapor pressure of steam in the bubbler at a specific water temperature. The temperature sensor and Arcon actuator amount to PI control over the thermodynamic equilibrium of the inlet gas mixture and liquid water phase in the steam box. The Antoine equation is of the form,

$$\log_{10}(P) = A - \frac{B}{T + C} \tag{5}$$

where the temperature (T) is in °C, and pressure is in bar. The corresponding A, B, and C values are 8.14, 1810.9 [°C], 244.5 [°C] for temperatures above 100 °C (Roizard, 2016).

All the sensors and actuators mentioned are connected to a LabVIEW interface shown in Fig. 3. The LabVIEW interface gets real-time data from the experimental setup, such as pressure, temperatures, potential, current, standard volumetric flowrates, gas concentrations, and can send signals to experimental equipment to modify parameters such as current set-point, the system back pressure, standard volumetric flowrates and steam box temperature set-point. The Compact Rio is run through a Field Programmable Gate Array (FPGA) script written in LabVIEW and the signals read through a 32-bit LabVIEW script. A Compact Rio cannot run with 64-bit LabVIEW, and a 32-bit LabVIEW cannot run Python scripts through a Python node. As a result, we run a 32-bit script to acquire data from the FPGA script connected to the Compact Rio and record the data to a text file each second. Simultaneously, the main script reads the text file to transfer the sensor data so that a Python script embedded into the LabVIEW interface can process the data. The built-in PI control function is used for all the PI-based control demonstrations in this research. For a model predictive control scheme, a code written in Python is incorporated into the LabVIEW interface.

In Çıtmacı et al. (2024), we have proposed a modeling approach and computationally demonstrated that this modeling approach can be used in a model predictive controller to operate the SMR system in an optimized way. In the present study, the modeling and control approaches are demonstrated to be experimentally effective. Still, there remains experimental challenges that prevent the application of the unmodified computational approach presented in Çıtmacı et al. (2024). Firstly, the gas products coming out of the reactor need to be cooled down to be processed by the GC. Water must also be removed from the GC feed since the peaks associated with water overlap with Ar and H_2 in the gas products signal. To this end, the outlet stream is exposed to a condenser that is cooled with a cold water stream and brings the gas mixture temperature to room temperature. This means that the unreacted steam in the tubular reactor is condensed and is not quantified by the GC. Any first-principle based model would need the steam flowrate to initialize the model or correct the model with respect to sensor measurements. Thus, in an experimental implementation, we need to account for the missing steam flowrate. Another difficulty is that the volumetric flowrate is needed to convert molar flowrates into concentrations through Eq. (6) for reaction rate calculations. The volumetric flowrate can be measured by flow sensors, such as a bubble meter; however, the experimental flow-meters do not operate at temperatures higher than 100 °C, and the outlet temperature of the SMR setup is expected to vary between 500 and 900 °C.

$$C_i = \frac{F_i}{q} \tag{6}$$

A final challenge is that the GC measurements are delayed by 18 min (15 min for gas separation, elution, quantification, and peak processing, and an additional 3 min for cooling of the GC). This makes it difficult to correct the model in real time and requires a solution to incorporate past measurements into the real-time modeling scheme. All of the aforementioned complications required a creative methodology, discussed in the following sections, to successfully implement model predictive control.

3. Catalyst synthesis

3.1. FeCrAl tubing pretreatment

All procedures for the Ni/ZrO_2 synthesis process and washcoat application were adopted from Richard (2021). Prior to the application of the ZrO_2 support and Ni catalyst, a Goodfellow FeCrAlloy © tube was washed with acetone and rinsed with deionized water to remove any

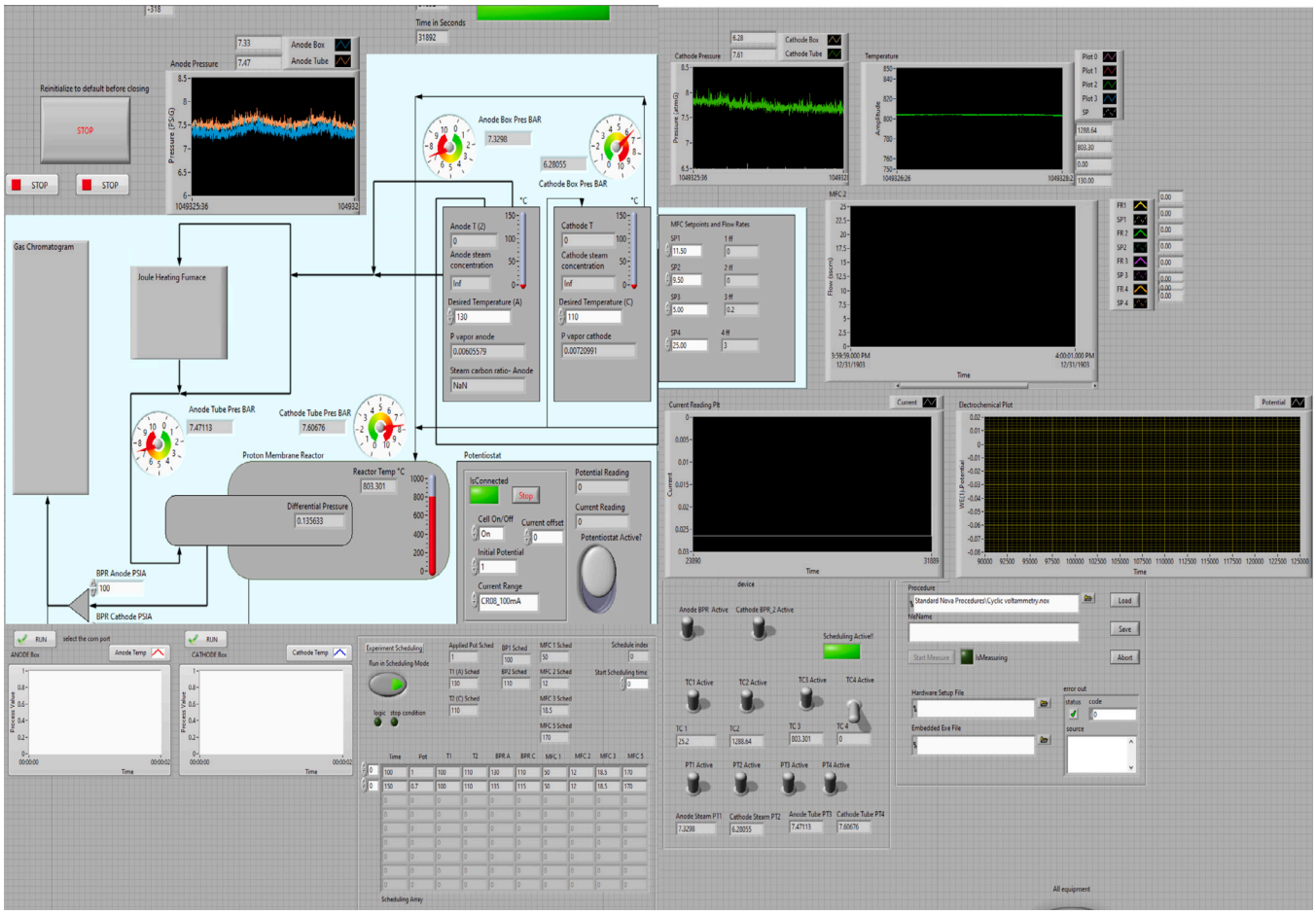

Fig. 3. Labview interface that connects sensors and actuators to the computer.

Fig. 4. FeCrAl alloy tube after first oxidation procedure at 950 °C for 10 h.

debris or other contaminants. The tube was heated to 950 °C in the furnace at a ramp rate of 1.4 °C/min where it was kept at the set-point for 10 h to calcinate the tube in air before being cooled to 30 °C at the previously mentioned ramp rate. During the heating process, slow dry air flowed through the system. The oxidation of FeCrAl reformer tubing is known to produce an adhesion-enhancing alumina layer on the inner and outer wall surface above 900 °C (He et al., 2020). The color change caused by the oxidation process was evident on the outer wall of the tubing in Fig. 4.

3.2. Washcoat slurry preparation and application

With respect to the washcoat slurry preparation, 15 ml of deionized water (Milli-Q IQ7000, Milliporesigma) was added to a 50 mL beaker housing a magnetic stir bar. The pH of the water was adjusted between 9–10 with ammonium hydroxide, (25% NH_3, 99.99% metal basis, liquid, Alfaesar) added dropwise. The pH-adjusted DI water was used to prepare a 21 wt % solution of zirconium (IV) oxide (powder, 5 um, 99% trace metals basis, Sigma Aldrich). The magnetic stirrer (Fisherbrand™ Ultra Thin Magnetic Stirrer) was set at 500 rpm and 4 g of ZrO_2 powder was added to the beaker and allowed to stir for 30 min. After stirring, the slurry was sonicated in a Tuttnauer Clean and Simple Ulrasonic 60 kHz sonicator for 20 min.

The tube was removed from the furnace and mounted vertically using clamps. A tee valve was installed at the top of the tube and a drain nipple was secured at the tube's bottom. The slurry was then poured down the inside of the tube and allowed to drain. After the slurry application, a PTFE tube was secured to the top of the tee and air was flown with a syringe pump at a rate of 1 ml/min for an hour. The tube was then inserted into the furnace and heated to 100 °C at a ramp rate of 1.4 °C/min. The tube was heated at this temperature for 1 h, then the temperature was ramped up to 500 °C (1.4 °C/min) and the tube was calcinated for 1 h. The temperature was ramped down to 30 °C at the same ramp rate. Five washcoats were prepared following the

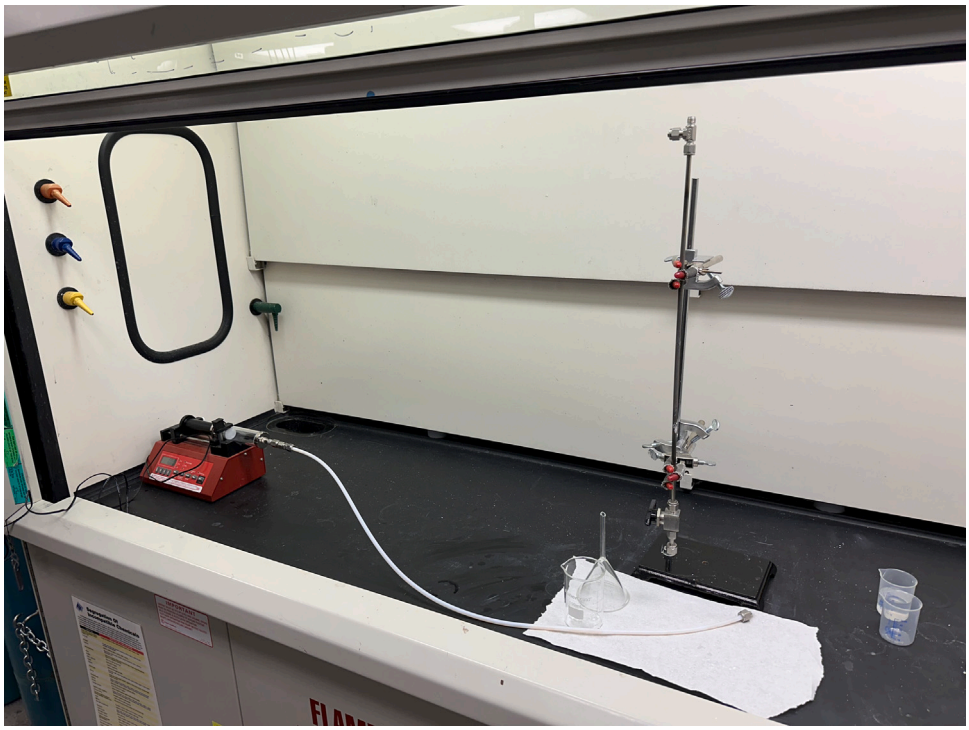

Fig. 5. Slurry application setup.

steps mentioned above. A final layer of the ZrO_2 support was added to the tube by leaving the slurry inside the tube for 10 h before drainage, followed by air drying and calcination (see Figs. 5 and 6).

3.3. Catalyst preparation

After calcination of the fifth ZrO_2 monolith, a 40 wt% nickel (II) nitrate hexahydrate (99.999% trace metals basis, Sigma Aldrich) was prepared and stirred in a 25 mL deionized aqueous solution for 5 min at 400 rpm. The solution was dropped into the vertical FeCrAl alloy tube via pipette and was allowed to sit for 1 min before being drained, dropwise, into a 100 mL beaker. Once the first nickel monolith was applied, the tube was air-dried for 30 min before undergoing calcination at 110 °C for 1 h, then at 500 °C for 1 h (1.4 °C/min). A second nickel monolith was added to the reactor tube and remained in the tube for 12 h. Following the draining of any residual nickel nitrate, calcination was performed once more with the previous procedure. The estimated loading of Ni on ZrO_2 is 50–80 mg.

3.4. Catalyst reduction

A proper reduction technique was developed to initialize the catalytic activity of Ni/ZrO_2 before each experiment. For reforming, reduction of the Ni surface sites with high temperature H_2 reverts any metal oxides into their original metallic forms, thereby regenerating the catalyst. For this reason, the reduction procedure was performed 12 h prior to every steady-state, PI-control, and MPC experiment.

An ATS cylindrical heating element, coupled with a PI temperature controller, served as the heating element for the reduction procedure. The first step of the procedure increased the temperature of the reactor tube to 110 °C (at a rate of 5 °C/min). After 1 h at 110 °C, the PI controller ramped up the reactor temperature to 850 °C (at a rate of 5 °C/min) where it remained for 4 h. Subsequent cooling to 20 °C occurred at the previous ramp rates. Constant flows of N_2 and H_2 (96 sccm and 64 sccm, respectively) were maintained throughout the temperature schedule. After reduction, and prior to the start of any experiment, the catalyst was preserved with low-flowing N_2 and H_2 (30 sccm and 17.7 sccm, respectively).

4. Feedback control for experimental data collection

The experimental SMR system requires a controlled increase of the temperature to prevent harming the catalyst. At the same time, it offers an opportunity for controlling gas phase concentrations with a PI controller since the GC measurements are needed to generate data that can be used for model development.

4.1. Temperature control for data collection

As discussed in Çıtmacı et al. (2024), the temperature increase should be limited to 6 °C/min to prevent catalyst degradation. If the reformer temperature rapidly increases or decreases, a change in the crystal structure of the catalytic monolith may occur by sintering and bring about changes to the Ni/ZrO_2 surface and bulk morphologies. The suggested constraint is around 6 °C/min and the temperature ramping trend should be linear. Since the temperature and current relationship is not linear (explained in detail in Section 6), a constant increment in current would cause more than 6 °C/min at the higher temperature range. Thus, PI control can manipulate the power supply current to increase/decrease the reformer temperature in gradual increments.

An additional constraint is used to limit the gain of the current-controller in order to generate a linear increase in the reformer temperature when approaching the temperature set-points. If the current-controller is too aggressive, a 6 °C/min temperature set-point increase may result in a significant initial jump in current, and 60%–80% of the final set-point value is achieved in the first few seconds of controller action. In this case, the controller continues to slowly decrease the current over the next few minutes to remain at the temperature set-point. Even though the average ramp rate may be within the °C/min constraint, the release of large amounts of electrons during the initial

Fig. 6. Wet ZrO_2 washcoat monolith at the end of FeCrAlloy reformer tube prior to calcination and Ni catalyst embedment.

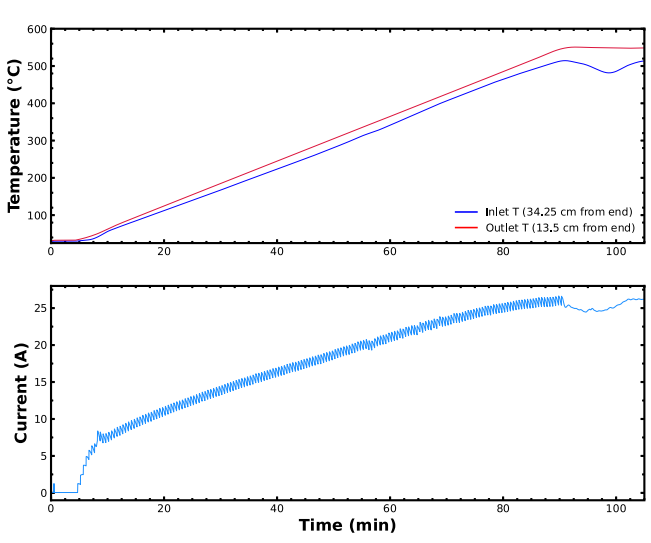

(a) Start-up phase reactor temperature increase.

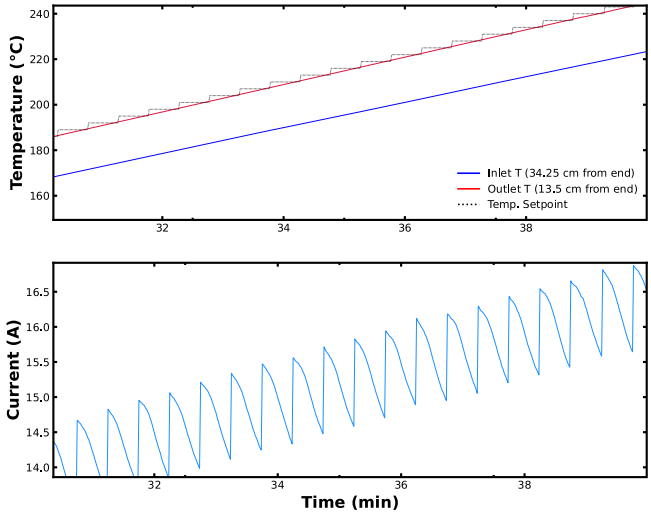

(b) Zoomed in set-point change for linear temperature increase.

Fig. 7. Linear temperature increase under control and corresponding current manipulation.

time steps of controller action leads to a sharp increase in the temperature derivative, violating the temperature rate of change constraint, and possibly inhibiting Ni surface sites by promoting sintering processes. Thus, to keep the temperature derivative constant at 6 °C/min, the current should not change more than 2 *A* in one time-step. As it is explained in Section 6.2, 1 *A* increase in the current can lead to an increase of up to 39 °C (if a final steady-state is reached). However, the way that the controller works is that it first causes a sharp increase in the current within 1 to 2 *A*, after which the current gradually decreases to preserve a linear change in temperature (see Fig. 7).

4.2. Steady-state data collection

Following the tuning of a controller to linearly increase the reactor temperature, experimental data at specified temperatures were collected to determine the SMR reaction kinetics and to quantify radial heat transfer. A range of thermal conditions were designated as steady-state set-points. The temperature was slowly increased to those temperatures and multiple GC injections were made at a steady-state temperature, and subsequently, the PI controller drove the process to the new temperature target. To limit the deactivation of Ni/ZrO_2

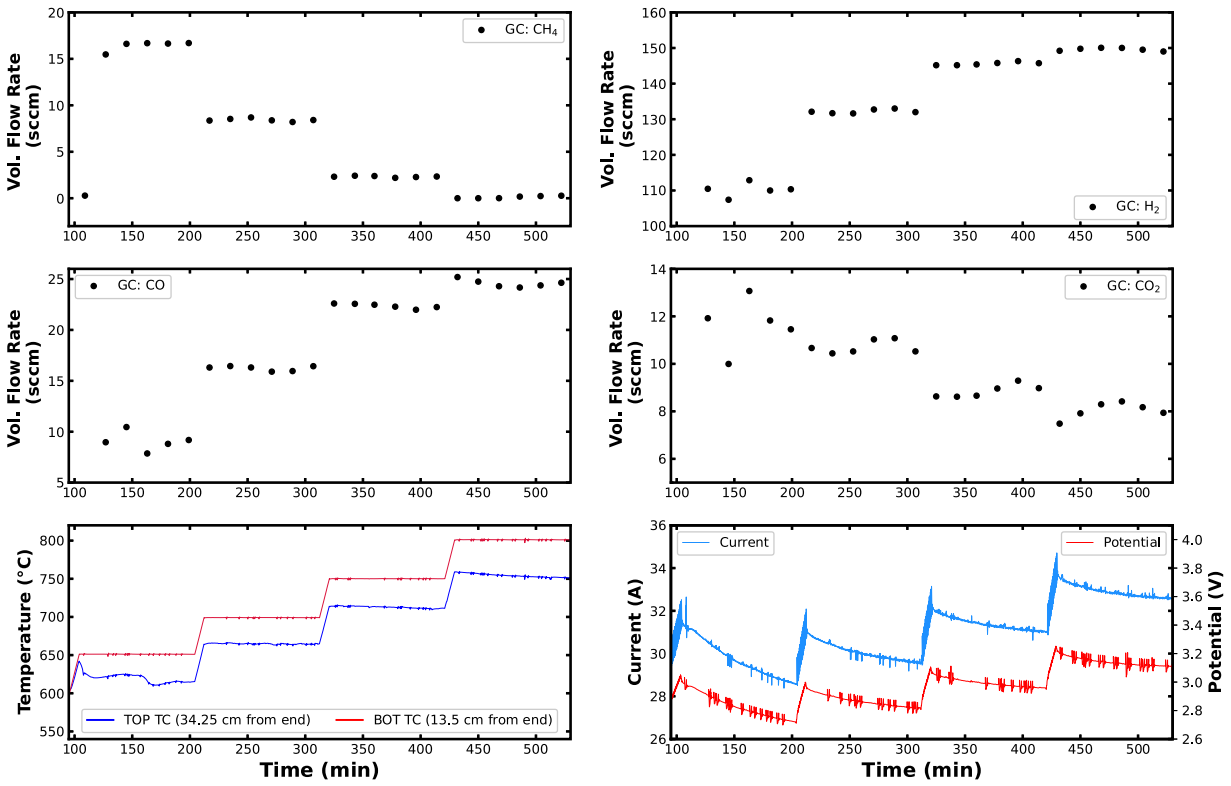

Fig. 8. Steady-state data collection with a Joule-heated energy source for experimental parameter calculations. Temperatures range from 650 °C to 800 °C for the outlet thermocouple. Each steady-state condition was maintained for 110 min.

catalyst, the PI controller was used to drive the outlet temperature of the reactor from 550 to 800 °C in increments of 50 °C gradually over a certain time window. The corresponding current ranges between 23 A to 34 A depending on the heat transfer coefficient. However, Fig. 8 demonstrates that, after the controller drives the reactor temperature to a new set-point temperature, the current is gradually decreased to keep the temperature at the set-point. This would suggest that the system is not at a thermal equilibrium as long as the current keeps decreasing. The main reason for this is the fiberglass insulation that surrounds the tubular reactor. The heat conduction from the surface of the reactor to the fiberglass is very slow since fiberglass has a very low heat conduction coefficient. As a result, the increase on the fiberglass surface temperature is not as fast as the temperature increase on the reactor outer wall. When the reactor wall is driven to a steady-state temperature, the insulation is at a lower temperature due to slow heat conduction. As the controller keeps the reactor wall temperature constant, the fiberglass slowly continues increasing in temperature, resulting in lower heat loses as time progresses. Hence, the controller reduces the current input to the reactor to keep it at a steady temperature. This is an indication that the heat transfer coefficient for the heat lost to the surroundings is not constant. Also, a large temperature difference in excess of 50 °C was seen between the reformer's inlet and outlet after the start of the endothermic SMR reactions that consume heat at the inlet section.

A feed mixture of CH_4, H_2O, H_2, and Ar (39.47/119.5/17.7/6.47 sccm) was sent to the reactor at 1 atm for all steady-state and dynamic control experiments. Each steady-state temperature was maintained for 110 min, giving ample time for kinetic equilibrium to occur and for the minimization of thermal gradients in the reactor insulation. The high temperature data collection experiment is shown in Fig. 8. Six flowrate samples from the GC were averaged at each temperature to determine the steady-state effluent flowrates. When the outlet temperature of the reformer tube was 500 °C, the conversion of methane was 7%, compared to 99% at 800 °C. Above 650 °C, the reverse WGS reaction is favored, leading to greater CO selectivity over CO_2. Fig. 10 confirms this activity and the maximum selectivity towards CO_2 production occurs at 650 °C when the ratio of CO_2:CO is 1.31 (Fig. 9(b)). The average hydrogen production rate at 800 °C was 149.6 sccm, and the average absolute errors between the computational model of Çıtmacı et al. (2024) and laboratory results in Fig. 10 were 1.59, 3.43, 1.45, and 2.47 sccm for CH_4, H_2, CO, and CO_2, respectively. Most of the variability in H_2 measurements occurred at the 650 °C and 700 °C steady-states. The high error is attributed to increasing catalyst deactivation coupled with axial and radial thermal gradients introduced by catalytic inhibition. Experimental errors in the GC total mixture percentage also peaked around the 650 °C and 700 °C steady-states, leading to additional variability in the measurements of all gas species at these temperatures. The GC total mixture percentage should equal 100% for a perfectly calibrated system. In practice, it is found that the total mixture percentage is somewhere between 101%–105%, as shown in Fig. 12.

The thermodynamic efficiencies for steady-state conversion of CH_4 at 650, 700, 750, and 800 °C outlet temperatures are given in Table 1. CH_4 is initially an energy carrier and the efficiency of transforming CH_4 into H_2 is an essential metric for the overall SMR process. Heats of reaction for steam methane reforming were calculated using the heat capacities (C_P) for all reactants and products of the first SMR reaction. Similarly, the enthalpy required to heat the inlet gases to the average reformer temperature was calculated by integrating their respective C_P values over the temperature differential between the laboratory conditions and the inside of the reformer. The efficiency calculation is given by the following equation (see the Eq. (7) in Box I): where the thermodynamic efficiency of CH_4 conversion is equal to the ratio of the heat of reaction for the first SMR reaction at a given steady-state temperature times the molar flowrate of converted CH_4 plus the energy requirement to heat the inlet gasses to the steady-state temperature over the average power input. An optimal thermodynamic efficiency of 10.69% was achieved for the electrified SMR system at the 730 °C

Table 1
Thermodynamic reaction efficiency for steady-state CH_4 conversion rates.

	Average reformer temperature (°C)			
	632	681	730	776
$\Delta H_{T,\ SMR}$ (kJ/mol)	232.46	235.5	239.01	242.81
CH_4 conversion energy requirement (W)	4.79	5.98	6.82	7.09
ΔH for inlet gases (W)	2.74	2.96	3.21	3.43
Average power input (W)	84.51	86.58	93.81	103.39
CH_4 thermodynamic reaction efficiency (%)	**8.91**	**10.33**	**10.69**	**10.18**

$$e_{ff} = \frac{\Delta H_{\text{T, SMR}} \times (\text{CH}_{4,\text{ Molar flowrate In}} - \text{CH}_{4,\text{ Molar flowrate Out}}) + \Delta H_{\text{Inlet Gasses}}}{Average\ Power\ Input} \times 100\% \tag{7}$$

Box I.

steady-state condition. This corresponds to an outlet temperature of 750 °C, an average CH_4 conversion of 94.1%, and a CO2:CO ratio of 0.396. The 681 and 776 °C steady-states generated efficiencies over 10% as well, signifying the relative optimality of the 700 to 800 °C outlet temperature range.

The experimental electrified SMR system includes an ATS split-tube electric furnace. To confirm the proper workings of the Joule-heated reformer, the electric furnace was used as a standard for comparison. The heating profile of the electric furnace is axially parabolic, with the center of the furnace holding the peak temperature set by the Watlow PI controller using an Omega K-type heavy duty thermocouple for temperature sensing. As a result, the heat profile was at a minimum at the inlet and outlet of the reformer. Except for the ATS specification limits of 1100 W, 115 V, and 9.6 A, the real-time power output of the electric furnace was not known during steady-state data collection. In spite of this, it was expected that the steady-state CH_4 conversion and CO_2:CO selectivity should be comparable to the Joule-heated energy source given that the average temperatures of the two heating elements were within 20 °C. The CH_4 conversion for both heating elements was 100% at 800 °C and 94% at 750 °C, indicating identical catalytic performance at the upper operational limits of the reformer. At 650 and 700 °C, the electric furnace converted 5% and 3% more CH_4 than the Joule-heated furnace which was within the range of experimental error (Fig. 9(a)). Thus, the Joule-heated reformer adequately supplied energy to the outer reactor shell in the form of heat. Additionally, the CO_2:CO selectivity for the heating elements was comparable for all steady-state measurements (Fig. 9(b)), except for 650 °C which produced selectivities of 1.35 and 1.04 for the Joule-heating system and the electric furnace system, respectively. A difference in shape of the heating profiles of the heating elements may have caused the deviation in CO_2 products between the two experiments. It is also possible that catalyst deactivation may have influenced the SMR reaction rates during the electric furnace experiment.

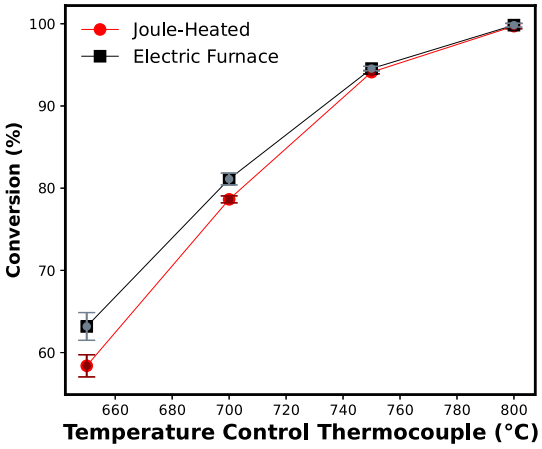

(a) Average steady-state conversion when the temperature ranges from 650 °C to 800 °C.

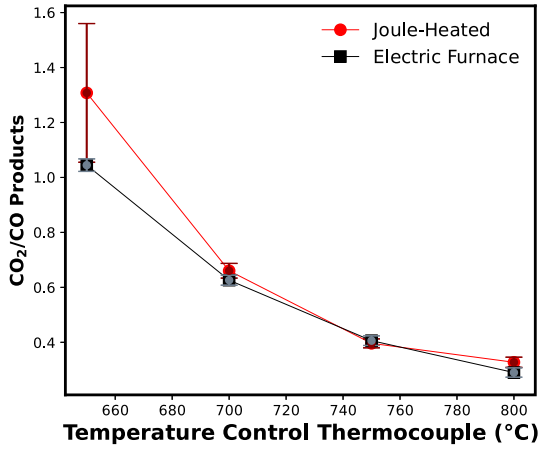

(b) CO_2/CO product selectivity over the same temperature range.

Fig. 9. Steady-state data collection from two energy sources: Joule-heated setup and electric furnace setup.

5. Modeling

5.1. Lumped parameter model

Real-time MPC of the SMR system requires a model that can be solved sufficiently fast in real-time on the order of seconds. SMR reactions occur in a tubular flow reactor, which would require solving partial differential equations (PDEs) to account for spatio-temporal evolution of variables such as species concentrations and temperature. Solving PDEs require commercial CFD software (e.g., Ansys Fluent, Comsol, etc.) and the solution time may be on the order of hours to days depending on the model detail. Thus, building an MPC based on a CFD model is not appropriate for real-time control purposes. In order to efficiently solve the mass and energy balance equations in real-time, the flow reactor is approximated as a continuously stirred tank reactor (CSTR) modeled by a lumped parameter ordinary differential equation (ODE) system, which is much faster to solve with methods like Runge–Kutta or Explicit/Implicit Euler. This brings a trade-off between the accuracy of the ODE model solution and numerical simulation speed. A

lumped parameter approach sacrifices some accuracy in the resulting model as it does not account for spatial variations of the process state variables but it enables real-time solution calculations with a sufficient accuracy. Below, the lumped parameter model equations are given; the derivation of the lumped model can be found in Çıtmacı et al. (2024).

The reaction mechanisms of SMR on Nickel-based catalyst were investigated by Xu and Froment (1989), from which the reaction rate equations were as follows:

$$r_{1,SMR} = \frac{k_1}{P_{H_2}^{2.5}} \cdot \frac{P_{CH_4} \cdot P_{H_2O} - \frac{P_{H_2}^3 \cdot P_{CO}}{K_1}}{(DEN)^2} \tag{8a}$$

$$r_{2,WGS} = \frac{k_2}{P_{H_2}} \cdot \frac{P_{CO} \cdot P_{H_2O} - \frac{P_{H_2} \cdot P_{CO_2}}{K_2}}{(DEN)^2} \tag{8b}$$

$$DEN = 1 + K_{CO} \cdot P_{CO} + K_{H_2} \cdot P_{H_2} + K_{CH_4} \cdot P_{CH_4} + K_{H_2O} \cdot \frac{P_{H_2O}}{P_{H_2}} \tag{8c}$$

$$k_j = A_j \cdot \exp\left(-\frac{E_j}{R \cdot T}\right), \quad j = 1,2 \tag{8d}$$

$$K_i = A_i \cdot \exp\left(-\frac{\Delta H_i}{R \cdot T}\right), \quad i = CH_4, H_2O, CO, H_2 \tag{8e}$$

and the mass balances for our electrified SMR system are as follows:

$$\frac{dC_{CH_4}}{dt} = \frac{1}{V_R}\left(F_{CH_4,0} - r_1 \cdot W - q \cdot C_{CH_4}\right) \tag{9a}$$

$$\frac{dC_{H_2O}}{dt} = \frac{1}{V_R}\left(F_{H_2O,0} - (r_1 + r_2) \cdot W - q \cdot C_{H_2O}\right) \tag{9b}$$

$$\frac{dC_{CO}}{dt} = \frac{1}{V_R}\left((r_1 - r_2) \cdot W - q \cdot C_{CO}\right) \tag{9c}$$

$$\frac{dC_{H_2}}{dt} = \frac{1}{V_R}\left(F_{H_2,0} + (3 \cdot r_1 + r_2) \cdot W - q \cdot C_{H_2}\right) \tag{9d}$$

$$\frac{dC_{CO_2}}{dt} = \frac{1}{V_R}\left(r_2 \cdot W - q \cdot C_{CO_2}\right) \tag{9e}$$

$$\frac{dC_{Ar}}{dt} = \frac{1}{V_R}\left(F_{Ar,0} - q \cdot C_{Ar}\right) \tag{9f}$$

The solution of the above equations require to express the molar flowrate (F_i) in terms of concentration (C_i) and volumetric flowrate (q). Specifically, the volumetric flowrate will vary based on temperature as in Eq. (10) (Çıtmacı et al., 2024) below:

$$q = \frac{F_{T0} + 2 \cdot r_1 \cdot W}{\frac{P}{RT}} + \frac{V_R}{T} \cdot \frac{dT}{dt} \tag{10}$$

5.2. Model initialization

Molar and volumetric flowrates for steam are not measured via measurement sensors. Still, using the available flow equations, the following equations can be solved simultaneously with a good initial guess for the steam molar flowrate:

$$0 = q - \frac{FRT}{P} \tag{11a}$$

$$0 = q - \frac{F_{T0} + 2 \cdot r_1 \cdot W}{\frac{P}{RT}} - \frac{V_R}{T} \cdot \frac{dT}{dt} \tag{11b}$$

where F is the total flow rate, Eq. (11a) is the ideal gas law and Eq. (11b) is the expression of the volumetric flowrate. The first reaction rate (r_1) is a function of gas species partial pressures including steam, which is shown in Eq. (8a). Eq. (12) below can be utilized to calculate the partial pressure of each species required in the rate equation:

$$P_i = \frac{F_i}{F_T} P \tag{12}$$

where F_i and P_i are molar flowrate and partial pressure of each gas species, respectively. These equations can be used to initialize the ODE solver of the process dynamic model at a steady-state. The molar flowrates are obtained from the GC-based calculations, while temperature values are measured by the two thermocouples. Once the system reaches steady-state, the total volumetric flowrate (q) and the steam flowrate (F_{H_2O}) are calculated, and the ODE solver is initialized to calculate the rest of the process variables.

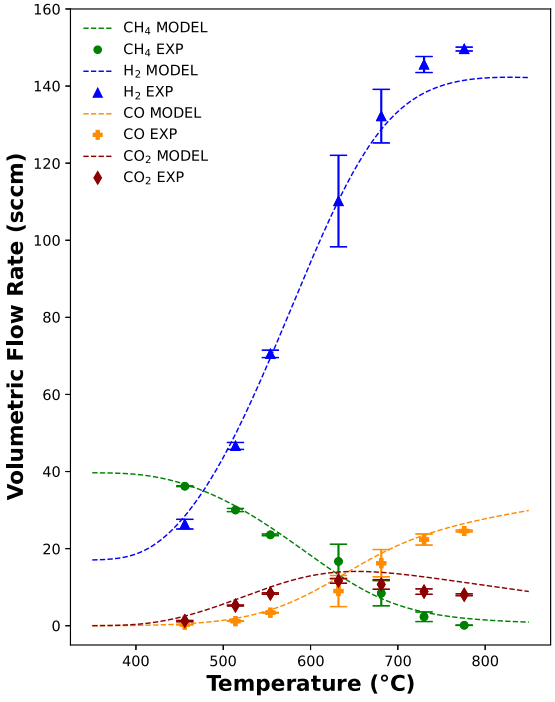

Fig. 10. Steady-state experimental data and model predictions over the 400 °C to 800 °C temperature range. For the experimental dataset, average steady-state temperatures are reported. Error bars represent the standard deviations of volumetric flowrates.

5.3. Parameter estimation using experimental data

Our previous computational study in Çıtmacı et al. (2024) suggested an approach for using a lumped parameter model in a model predictive controller that does not use the thermodynamic energy balance for temperature estimation, rather it uses a data-driven first-order dynamical model that relates the applied current to the reactor temperature. However, due to the nonlinear nature of heat transfer in steam methane reforming, first-order linear dynamic models can only capture the reactor temperature behavior within the region where the linear model is valid. To create a more accurate model over the entire operational temperature range, a comprehensive energy balance is used in the present work. Using a lumped parameter assumption, the energy balance takes the following form:

$$\frac{dT}{dt} = \frac{I^2\bar{R} + \sum_i \dot{m}_{p_i} C_{p_i}(T_{p_i} - T) - W r_{SMR} \Delta H_{SMR}(T) - W r_{WGS} \Delta H_{WGS}(T) + UA(T_s - T)}{\sum_i \rho_i C_{p_i} V} \tag{13}$$

where the $I^2\bar{R}$ term represents the heat given to the system by the power supply and can be read from the sensors. The reaction enthalpies at specific temperatures can be calculated mathematically using the Shomate equation (Shomate, 1954) which accounts for the heat capacity and formation enthalpies at standard state (298 K, 1 atm). The reactor is cooled by the surrounding ambient temperature, which is accounted for in the $UA(T_s - T)$ term. Thus, the only unknown in the energy balance is the UA term, which is the overall heat transfer

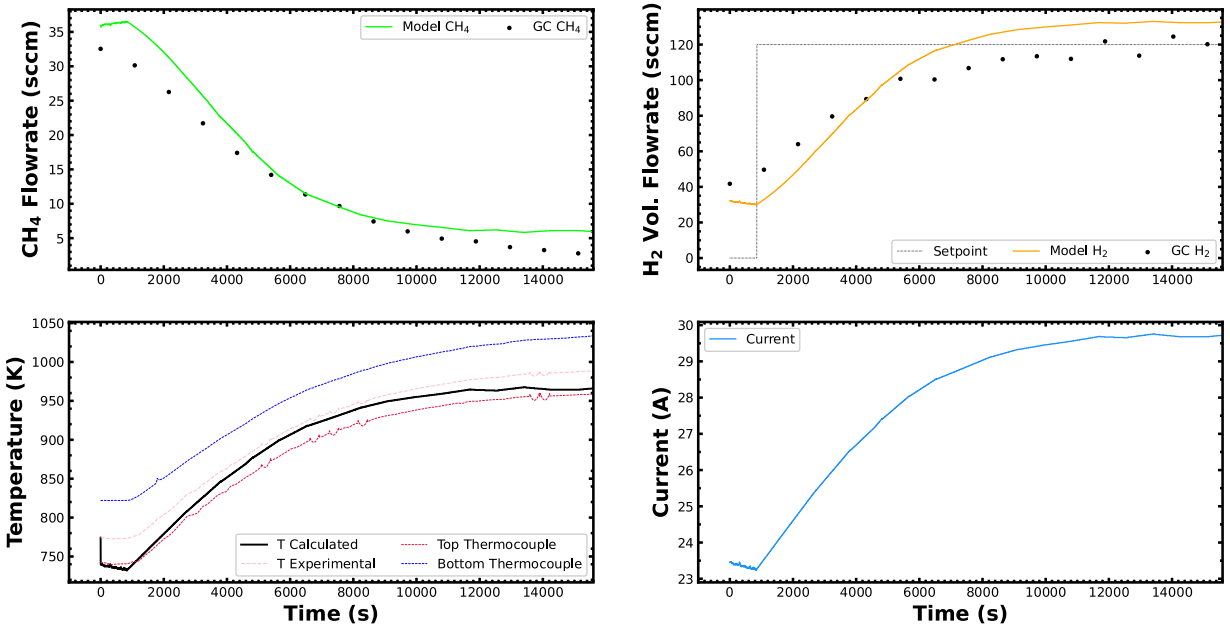

Fig. 11. Model predictions for outlet CH_4 and H_2 molar flowrates when experimental current is provided.

coefficient times the heat transfer area. In a perfectly insulated system, the U term would be zero and the system would not lose any heat to the surroundings. In that case, there must be a cooling stream, such as a jacket, around the reactor to reduce the reactor temperature when necessary. Furthermore, experimental systems are not ideal systems, and despite the use of an insulation layer in our reactor, there are heat losses to the surroundings. The UA term can be estimated by fitting experimental temperature data to the mass and energy balances, Eqs. (9) and (13), respectively. To fit the data, steady-state operating data, such as the experimental data shown in Fig. 8, can be used directly without de-noising. Fig. 8 illustrates the conditions for four steady-states at 650 °C, 700 °C, 750 °C, and 800 °C. Thus, this data is fitted to nonlinear mass and energy steady-state balances to estimate the UA value (Cui et al., 2024). As a result of the data fitting procedure explained in Cui et al. (2024), the UA term is estimated to be 0.116 J (s K)$^{-1}$. Finally, in our previous work (Cui et al., 2024), we demonstrated the fitting of the experimental data to the reaction kinetics equation described by Xu and Froment (1989) to estimate the pre-exponential factor and activation energy, and the results showed very close correspondence (see Fig. 10).

5.4. Model evaluation

The model predictive controller will use the lumped model described in Section 5.1. This model assumes that the mixing is perfect and the temperature and concentration profiles are uniform everywhere in the reactor. Note, in a tubular reactor, the reactions occur in the axial direction and neither the temperature nor the concentrations are uniform. The gas mixture starts reacting in the inlet section of the reactor where the highest heat consumption occurs due to the endothermic SMR reaction. This causes a significant temperature drop at the inlet section of the reactor which is evident when analyzing thermocouple values over the axial length of the reactor. The maximum temperature difference over this length is around 100 °C. This brings about the question of which temperature to use in the lumped model. One effective approach is taking a weighted average of top and bottom thermocouples to be the lumped model temperature.

To find meaningful weights for averaging the reactor temperature, available data from flowrate feedback control were used. In this instance, various weights were used to find the best matching outlet

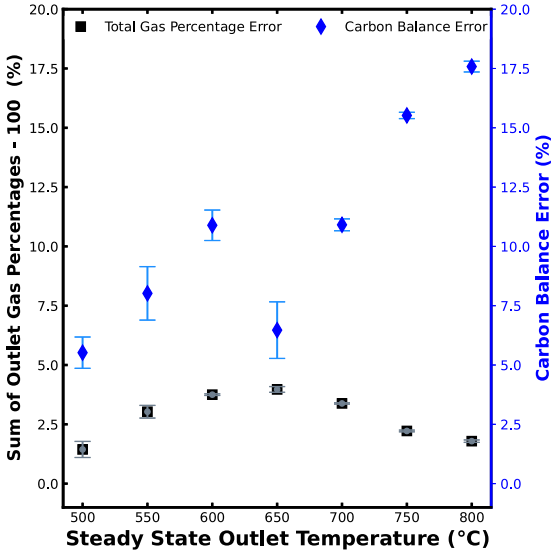

Fig. 12. Average carbon balance and GC errors for the steady-state data collection experiments shown in Fig. 10.

flowrate and temperature prediction. Since the heat transfer coefficient term (UA) was known, providing the experimentally recorded current values to the energy balance equation (Eq. (13)) was sufficient to estimate the reactor temperature. The estimated temperature was subsequently compared to the weighted average of experimentally recorded inlet and outlet thermocouple values.

To compare the model predictions with recorded thermocouple temperatures and GC concentrations, the numerical ODE solver that integrates the mass and energy balances (Eqs. (9), (13)) is provided with an initial condition. However, the gas chromatogram provides only molar flowrates of CH_4, H_2, CO, CO_2, and Ar. Steam concentration is not measured in the reactor effluent as steam is condensed before the GC feed. As a consequence, initializing the ODE solver requires estimates for the outlet steam molar and volumetric flowrates. The two equations shown in Eq. (11) were solved simultaneously for a given

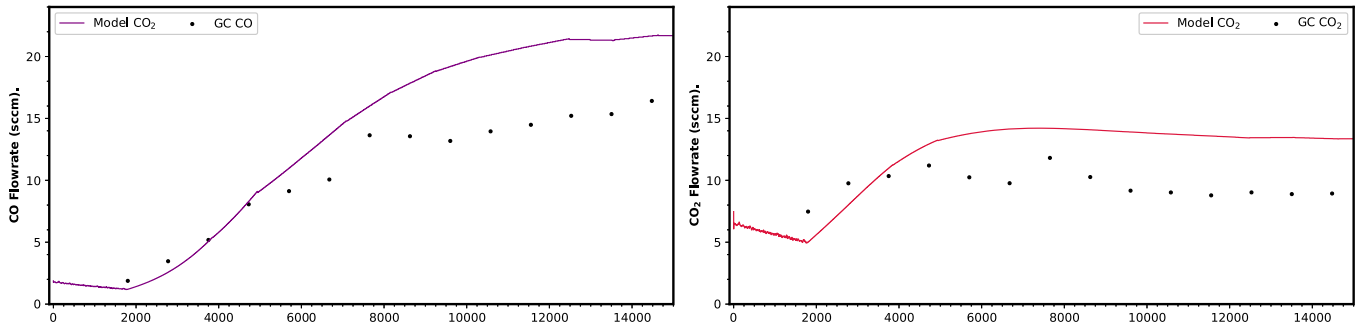

Fig. 13. Model predictions for CO and CO_2 when experimental current is provided. The CO_2 flowrate estimations demonstrate some deviation from the experimental results, which might be due to coke formation at higher temperatures.

steady-state to get an estimate of outlet steam molar and volumetric flowrates. Once F_{H_2O} and q values are estimated, the solver can be initialized.

In each experiment, multiple GC injections are taken at each steady-state (5–6 injections per steady-state temperature). If the experiment performs flowrate control, the controller is initialized after multiple GC injections at the outlet section temperature of 550 °C steady-state. To find the top and bottom thermocouple weights, the model is initialized at the steady-states and integrated with respect to the recorded experimental current values. After trying many combinations of weights for the top and bottom thermocouples, the optimal weights are estimated to be 60% of the top thermocouple value and 40% of the bottom thermocouple value. This also corresponds to the vicinity of the experimental steady-state H_2 flowrate value at the weighted temperature. The overall temperature of the reactor for model calculations is based on these weights. Since the majority of CH_4 conversion occurs at the inlet section of the reactor, giving more weight to the top thermocouple provides a better representation of the reactor heat profile when compared to taking the arithmetic mean of the two thermocouple values. The model predictions with the respective weights are shown in Fig. 11, for one of the feedback control experiments later explained in Section 6.1. This model takes only recorded experimental current as an input, calculates temperature values, gives continuous predictions of the gas specie concentrations. The predictions are compared to discrete GC measurements in Fig. 11.

Remark 1. The UA term must be calculated with respect to the weighted average temperature. Thus, each weight tested with the experimental data must calculate a unique UA value. The data fitting of UA term shown in Section 5.2 is calculated for the weights obtained in this section.

5.4.1. Carbon formation effect

In any SMR system, a common disturbance process is the formation of carbon (coke) on the catalyst throughout the reactor. A carbon layer is formed on the catalyst and blocks available surface sites, decreasing the catalytic performance (Meloni et al., 2020). The side reactions that take place in Eq. (14) cause coke formation.

$$CH_4 \rightleftharpoons 2H_2 + C, \qquad \Delta H_{298} = 75 \text{ kJ mol}^{-1} \tag{14a}$$

$$2CO \rightleftharpoons CO_2 + C, \qquad \Delta H_{298} = -172 \text{ kJ mol}^{-1} \tag{14b}$$

This initially formed carbon, C_α, is very active and some carbon atoms are transformed to C_β. For C_β, atoms may be vaporized and the remaining portion can diffuse within the catalyst. This diffusion can make the carbon nucleate and precipitate at the back of the catalyst, causing the catalyst to lift, triggering fragmentation of nickel crystallite (Zhang et al., 2021). Coke formation is therefore detrimental to the catalyst and hard to avoid. When the carbon atoms are counted in the inlet stream (from CH_4) and outlet stream (from CO, CO_2, and unreacted CH_4). Fig. 12 demonstrates the difference for the steady-state data collection experiment in Fig. 8.

The carbon deposition effect can be reduced using methods like the gasification of the carbon layer to refresh the catalyst. As a part of the SMR system experimental procedure, H_2 and steam are used to gasify the carbon layer on the reactor catalyst for 5 min at the beginning and end of each experiment. However, coke formation may have caused deviations in modeling results due to carbon losses in the carbon mass balance for experimental data. Also, this phenomenon is very challenging to quantitatively model, and furthermore, it is difficult to eliminate coke while the SMR process is already running. Ginsburg et al. (2005) and Ashik et al. (2017) worked towards measuring the rate of carbon formation and proposed the rate equations shown in Eq. (14), which were developed under certain assumptions. For example, Ginsburg et al. (2005) assumed the decomposition of CO (Eq. (14b)) to carbon was dominant. However, both our steady-state and dynamic data do not support this assumption. If the coke formation is mainly caused by CO according to Eq. (14b), CO_2 flowrate estimation from the model should be smaller. However, CO_2 has larger estimated flowrate values when compared to the experimental data shown in Fig. 13, implying that this assumption may not be valid for our process.

6. Feedback control of hydrogen molar flowrate

6.1. Experimental PI control

In order to evaluate the efficiency of a model predictive controller in terms of speed of response, a control study with only sensor feedback is first conducted. In this control scheme, the controlled variable is the outlet H_2 flowrate and the manipulated variable is the current. As the SMR is an overall endothermic process, the equilibrium constant will increase as temperature increases, and the process will produce more H_2. The temperature controller drives the process from room temperature to the first steady-state at 550 °C in the bottom temperature, which corresponds to 500 °C in terms of the weighted average temperature. Then, the H_2 flowrate controller takes over and drives the process to the 120 sccm set-point decided in Cui et al. (2024). Theoretically, it requires 102.3 sccm of H_2 produced from the reaction (given that 17.7 sccm of H_2 is in the inlet flow rate to the reactor). According to the stoichiometric ratio of CH_4 and H_2 in Eq. (8), the minimum CH_4 consumption is 25.575 sccm if 4 moles of H_2 is produced from 1 mole of CH_4 (64.8% conversion), and maximum is 34.1 (86.4% conversion) sccm if 3 moles of H_2 is produced from 1 mole of CH_4 (excluding WGS reaction), respectively. However, it is important to note that this theoretical conversion range is calculated without considering the coke formation.

The inlet flowrates of CH_4, H_2O, H_2, and Ar remained unchanged from the steady-state experiments to maintain a gas hourly space velocity (GHSV) of 1000. Finally, after the set-point is reached and GC injections are taken for at least 324 min, the temperature controller

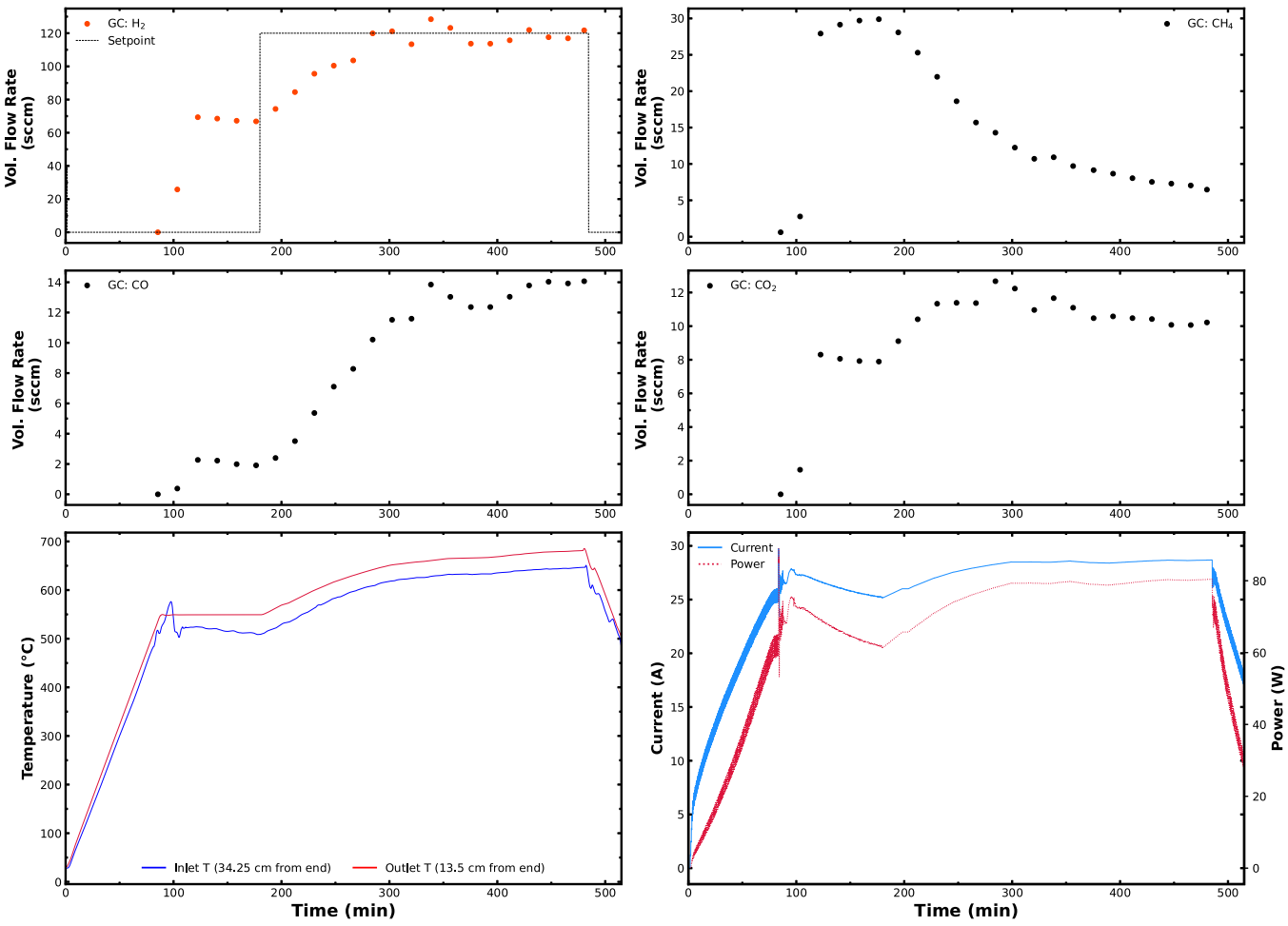

Fig. 14. First experiment under PI control based on GC feedback only.

takes over the process once more upon re-initialization in order to decrease the reactor temperature to ambient conditions. The GC data points are delayed by 15 min and updated every 18 min. Thus, the state seen by the controller is constant at the GC output for 18 min. However, the integral term in the controller keeps integrating the error, causing a continuous increase in the controller's current output being sent to the power supply on a per second basis. The controller was tuned in Cui et al. (2024) using a computational process model. The final parameters found from this simulation were $K = 0.0012$ A/sccm, and $\tau_I = 79$ s and have been adopted by the concentration PI controller. The results from the first PI control experiment are shown in Fig. 14. The control behavior is very consistent with the proposed control strategy in Cui et al. (2024). The controller drives the process to its 120 sccm set-point without violating the current ramp rate and keeps the process at said set-point with only slight fluctuations around the target hydrogen production value. The H_2 flowrate control experiment is repeated three times to show that this PI control scheme can drive the process at the desired set-point. The second experiment (Fig. 15) confirms the ability of the PI controller to drive the process to the desired set-point.

Fig. 17 demonstrates the error between the three PI control experiments and the closed-loop model under PI control prediction. This is an indication that the model would perform fairly well. The slight dynamic mismatch between 0 and 200 min might be due to the lumped parameter modeling. However, the mismatch at steady conditions between 300 and 400 min after the control starts might also indicate some other phenomena, especially for the third PI experiment.

While interpreting the result, it is crucial to note that the reverse water gas shift reaction is favored around the set-point. WGS reaction is slightly exothermic, and as the temperature increases the equilibrium shifts towards producing more CO and less CO_2 and H_2. Thus, at this point, the H_2 production is mainly maintained by the reforming reactions. At lower temperatures, 1 mole of methane produces roughly 4 moles of H_2, and as the reverse WGS takes over, 1 mole of methane produces 3 moles of H_2. However, as the temperature increases, the reforming reactions become faster and still produce more H_2 compared to lower temperatures. This phenomenon can be seen in Fig. 10. Around 650 °C, the CO_2 flowrate is decreasing while the CO flowrate is increasing. Also, after 650 °C, the slope of the H_2 flowrate production decreases as temperature increases. Thus, in the PI experiments, the set-point of 120 sccm is usually at a transition area for WGS and reverse WGS. Hence, after this point, the controller increases the reactor temperature to produce more H_2, converting more methane.

It is also very important to keep in mind that the scatter plots for each gas specie demonstrates when the GC measurement was taken and not when this measurement value was received by the controller. Thus, the controller keeps driving the process based on the previous GC result, and the integral term integrates the previous error. If the GC measurement is very close to the set-point, the controller tends to keep constant. However, as mentioned in Section 4.2, the constant current increases the temperature due to delayed heating of the fiberglass. Thus, while the controller thinks that the process is at steady-state, the gradual heating of the fiberglass is causing a temperature increase in the reactor, thus a surge in the H_2 concentration, even though the current seems to be constant. Moreover, the controller can start decreasing the current only after the GC measurement is obtained, meaning that the current was used for further increase of the H_2

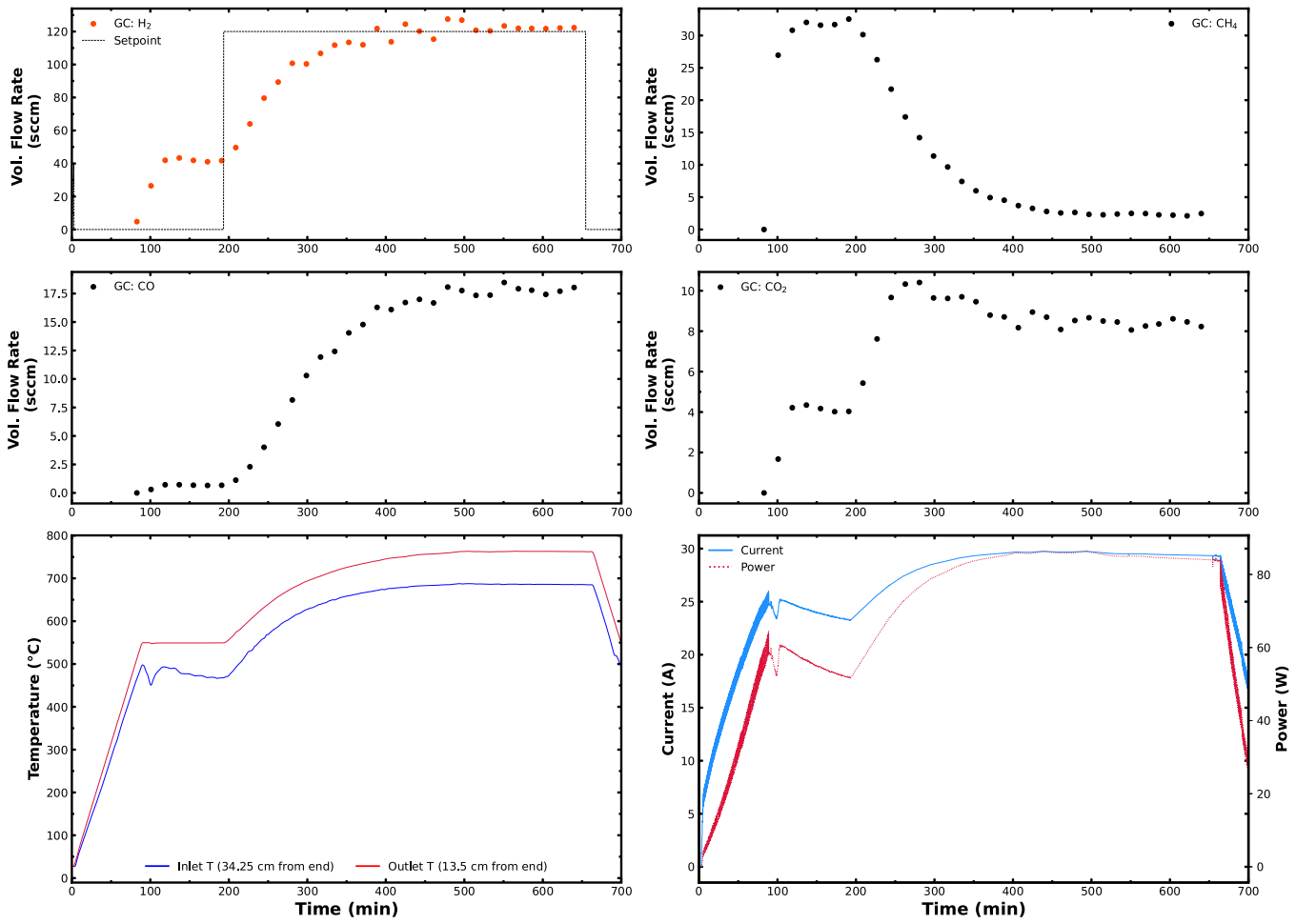

Fig. 15. Second experiment under PI control based on GC feedback only.

concentration when it should have decreased. One clear example of this is the H_2 flowrate increase in Fig. 16 at 420th and 450th minutes. To compensate for this increase, the controller quickly decreases the current, and this delayed control brings the process to a state before the reverse watergas shift reaction is favored. The further increase of the current triggers the reverse water gas shift and slows down the H_2 increase. This can be seen from the CO_2 concentration trend change at 265th minute, where the reverse WGS is triggered for the first time, and the 420th minute when the WGS reaction trend changes one more time.

The third experiment (Fig. 17) shows more variation as quantified in Table 2 in H_2 molar flowrate around the set-point. When CH_4 conversion is checked in Fig. 18, the H_2 flowrate is below the set-point, and yet, methane conversion approaches 100%. At this point, side reactions such as carbon formation (which is explained in Section 5.4.1) or catalyst deactivation might be happening in addition to reverse WGS shift reaction becoming more dominant. However, the PI controller still boosts the current to bring the H_2 concentration to the target value. These phenomena are not as severe in the first two PI control experiments, mainly because of the experimental conditions. The lumped parameter steady-state model suggests that the process settles at 120 sccm H_2 production rate around 650 °C (temperature weighted average). However, depending on the experimental variability of parameters (e.g., catalyst activity, coke formation, etc.), the steady-state temperature and reverse WGS triggering varies. The first PI control settles at the steady-state around 630 °C, and these temperatures are 715 °C and 695 °C for the second and third PI control experiments, respectively.

The difference between the inlet carbon flowrate (coming from CH_4) and the outlet GC measurements' carbon flowrate (coming from CO, CO_2, and unreacted CH_4) is shown in Fig. 19 with respect to time and temperature. Overall, an increase in reactor temperature causes a greater consumption of methane, and increases coke formation. At similar high temperatures, the third PI control experiment produced slightly higher amounts of carbon, which might indicate that the catalyst was more deactivated compared to the first two experiments. Instead of producing more H_2, the catalyst favors more carbon formation. Hence, a higher conversion does not mean higher H_2 production, since methane might be consumed for coke production.

The temperature increment is targeted to be kept under 6 °C per minute to preserve the catalyst activity. Thus, the PI controller was tuned to keep the catalyst under this constraint at all times. Fig. 20 displays the change in temperature each minute during the control experiments. The temperature change each minute is around 2.5 °C. A more aggressive controller gain could have been used for the PI for a faster response. However, even with the current parameters, the PI controller causes an oscillation in each experiment. Thus, a higher K_c value would lead to higher-amplitude oscillations which are undesired. Furthermore, these oscillations would become more severe as the deactivation and coke formation effects become more significant.

The PI control experiments demonstrate that a PI controller with delayed measurements requires between 120 to 200 min to drive the process to the set-point. Section 6 below focuses on the improvements on the response time using an estimation-based model predictive controller.

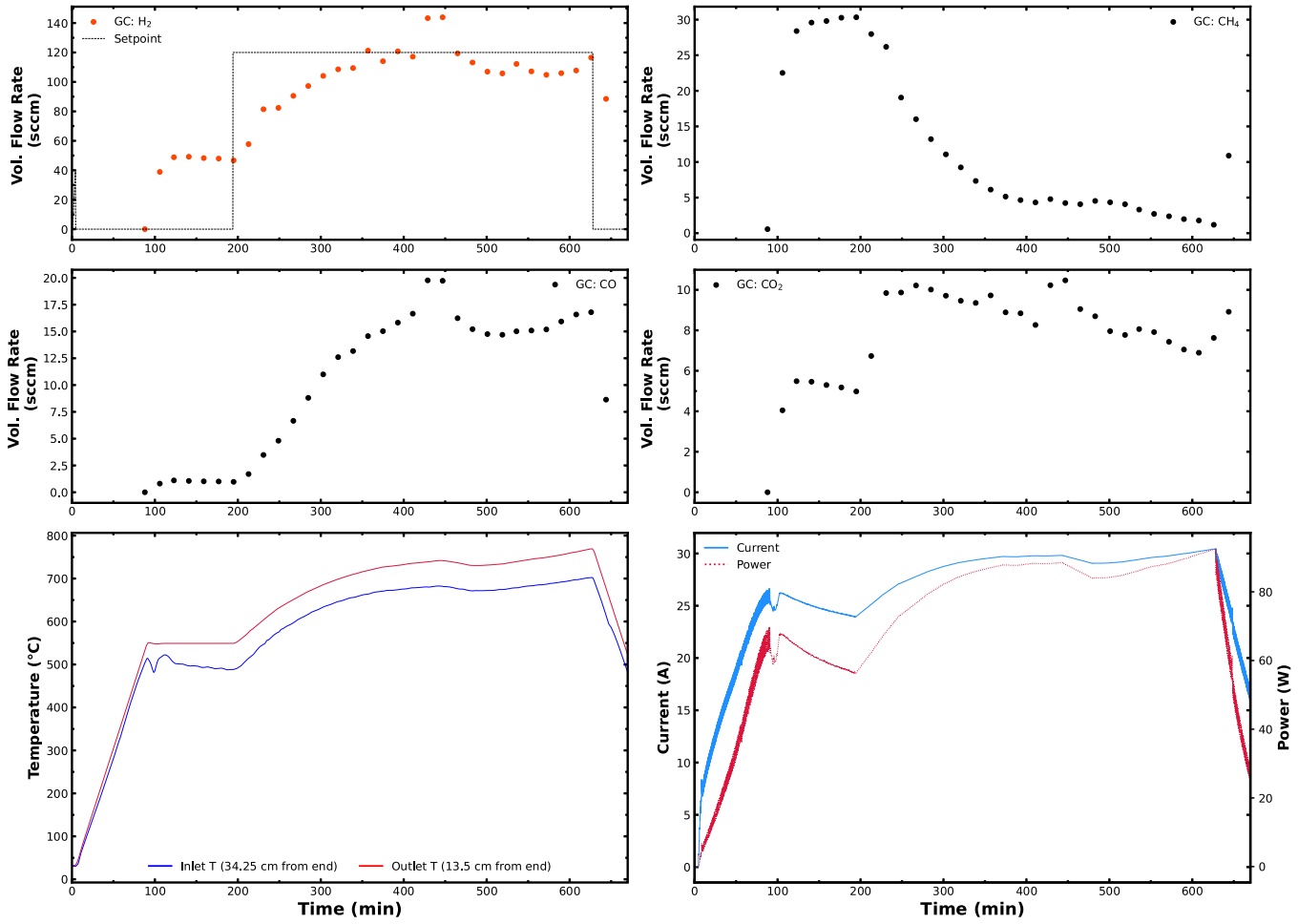

Fig. 16. Third experiment under PI control based on GC feedback only.

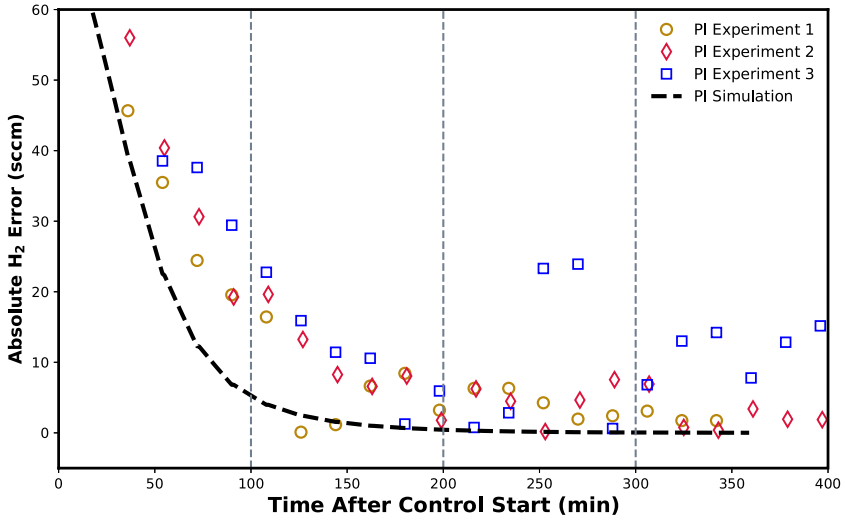

Fig. 17. Absolute error of H_2 (sccm) production with respect to simulated closed-loop response under PI control.

6.2. Model predictive control

The reaction kinetics are very fast for SMR reactions. The computational work done by Cui et al. (2024) demonstrates that the process is expected to settle at a steady-state within 1 s at 1000 GHSV. Thus, even for a slight temperature change, the time required for reaching a steady-state is very short. However, the allowed current increase rate prevents controllers from going to higher target temperatures to reach the desired production rates faster than the ramp rate limits. PI controllers might not provide the most optimal current input to the power supply at each time step. Instead, an MPC would ensure that the most optimal input value is calculated at each time step without violating

Table 2
Average absolute errors for hydrogen production (sccm) under PI control for different time intervals (min).

Time (min)	Experiment 1		Experiment 2		Experiment 3	
	Avg. Error (sccm)	St. Dev.	Avg. Error (sccm)	St. Dev.	Avg. Error (sccm)	St. Dev.
0–99	31.29	11.67	36.57	15.57	41.96	14.14
100–199	5.99	6.02	9.59	6.14	11.31	7.52
200–299	4.25	2.07	4.62	2.78	10.29	12.19
300–399	2.18	0.79	2.54	2.39	11.64	3.48

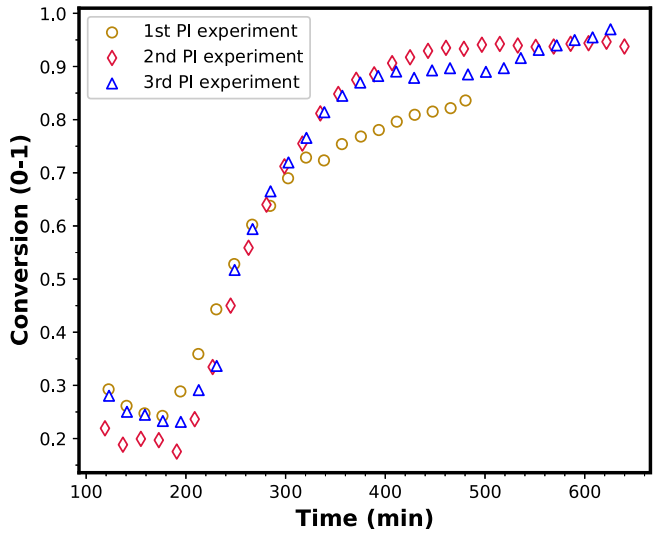

Fig. 18. CH_4 conversion for the 3 PI control experiments.

the constraints. Thus, we examine the behavior of an MPC to make sure that this process is driven to the desired H_2 production rate in the most efficient way possible. The model estimation and optimization are computationally inexpensive, such that all the calculations can be made on LabVIEW in one second. However, the LabVIEW script runs many calculations in one loop. Consequently, if a model solution calculation takes more than one second, there are delays on the code execution. To prevent these time delays in computing the control actions, the MPC is designed to make one calculation every 5 s.

The most important constraint given to the MPC is the 6 °C/min temperature change rate. This constraint is therefore embedded into the MPC optimization problem. To do this, the behavior of the temperature against current was examined experimentally. Using the process model explained in the previous section, a current against expected temperature graph is generated and fitted to a 2nd order polynomial. The resulting polynomial is $T(I) = 0.7I^2 + 2.64I + 290.7$ with an R^2 value of 0.99, and the data fit is shown in Fig. 21(a). The MPC operates between 700–1100 K, and thus, when zoomed into this operational region, it is possible to check if a linear constraint can be given. The data points in this region were fit to a linear function via regression, and the resulting function was found to be $T(I) = 39.4I - 186.2$, which is illustrated in Fig. 21(b). The data points show close alignment with the linear model. Thus, within this operation region, it is safe to assume that a 1 A increase in current causes a 39.4 °C increase in temperature. Since the MPC is designed to make a calculation every 5 s, the maximum allowed increase in current corresponds to 0.13 A to satisfy the 6 °C/min temperature rate of change constraint used in the MPC optimization problem.

6.2.1. Extended Luenberger observer

In the MPC architecture, the model predictions are updated with feedback obtained from real-time process measurement data. However, the measurement sensors do not yield volumetric and steam molar flowrates. In this type of a feedback control problem, methods like Kalman Filter (Kalman, 1960) or Luenberger observer (Luenberger, 1964) help to combine the process model and sensor feedback values to obtain an estimate of the state of a system. Specifically, an extended Luenberger observer can be developed for a dynamic system of the form:

$$\dot{x} = f(x,u) \tag{15a}$$

$$y = h(x) \tag{15b}$$

where x is the state vector, u is the control input vector, $f(x,u)$ is a nonlinear vector function, y is the measurement vector, and $h(x)$ is the transformation vector function that transfers the state value to the measurable physical information. Specifically, the extended Luenberger observer has the following form:

$$\dot{\hat{x}} = f(\hat{x},u) + K_{ELO}(y - h(\hat{x})) \tag{16}$$

where $\hat{x}$ is the estimated state vector, y is the measured output, and K_{ELO} is the observer gain matrix designed to ensure the convergence of the estimated states $\hat{x}$ to the true states x.

In the implementation of the ELO to the experimental setup, the model predictions are corrected by adding the difference between estimated values and sensor values, all multiplied by a tuned gain value. In our work, tests on model predictions were performed to see if the model's predictions could be updated using only temperature values (sampled each second) and H_2 flowrate values from a GC analysis (sampled every 18 min). In this way, the missing values are estimated from the model and the correction terms bring all the estimations closer to their real values. The ELO state estimates are subsequently sent to the MPC to optimize the current input for the next sampling time (5 s). It is also important to note that the process model in MPC is not corrected by an estimation error term as future measurements are not available; rather, the ELO is used to calculate the process state variables needed to initialize the process model used in the MPC. The detailed derivation of the equations for ELO using the process model and the observer gain matrix is presented in Cui et al. (2024). The experimentally tuned gain matrix (K_{ELO}) used in this work is as follows:

$$K_{ELO} = \begin{bmatrix} -0.01 & 0.05 & -0.1 & 0.7 & 0.01 & 0.04 & 100 \\ 0.8 & -0.60 & 0.2 & 2 & 0.005 & 0 & 0 \end{bmatrix} \tag{17}$$

where the first row corresponds to the correction tuning values for the difference in temperature and its effect on each of the species and the temperature. Each column shows the tuned values that influence CH_4, H_2O, CO, H_2, CO, Ar and temperature. The difference in H_2 does not affect the temperature ODE, since the first row of K_{ELO} mainly accounts for the temperature correction. The second row represents the correction that is implemented for the difference between H_2 production estimation and GC value that corresponds to 15 min prior. This 15-minute delay causes jumps in the ELO predictions. Also, since the H_2 values correspond to those from 15 min before, the ELO gain matrix should not have large gain to correct for the gas species at the current time step. Finally, since the H_2 concentration is controlled and the only sensor feedback for H_2 is obtained from the GC, the ELO output for H_2 is tuned to be very close to the last GC measurement. Using the ELO, the MPC optimization problem implemented on our experimental setup is of the form:

$$\mathcal{J} = \min_{I} \int_{t_k}^{t_{k+N_h}} L(\bar{x}(t), I(t))\, \mathrm{d}t \tag{18a}$$

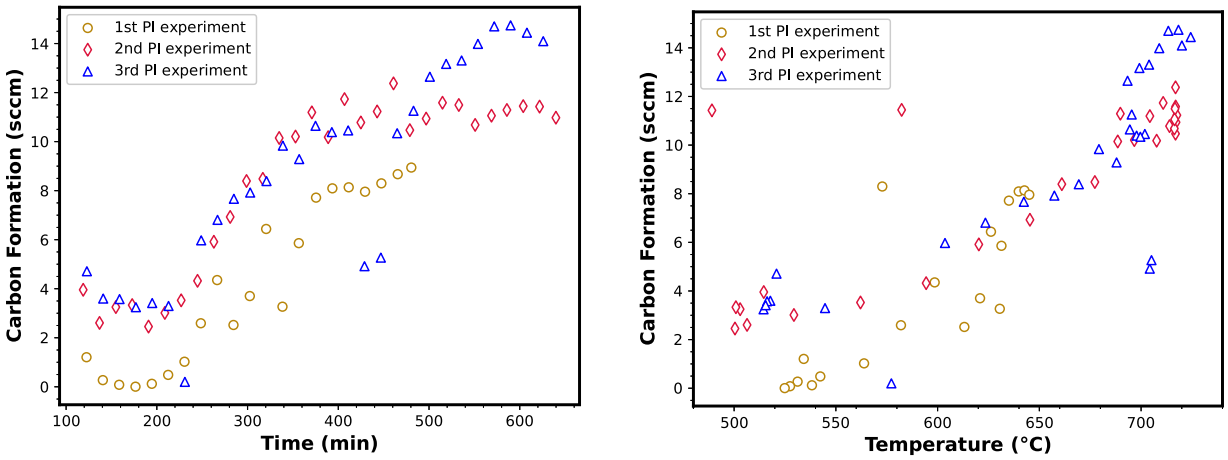

(a) Coke formation with respect to temperature.

(b) Coke formation with respect to temperature.

Fig. 19. Difference between the inlet and outlet carbon atom flowrates.

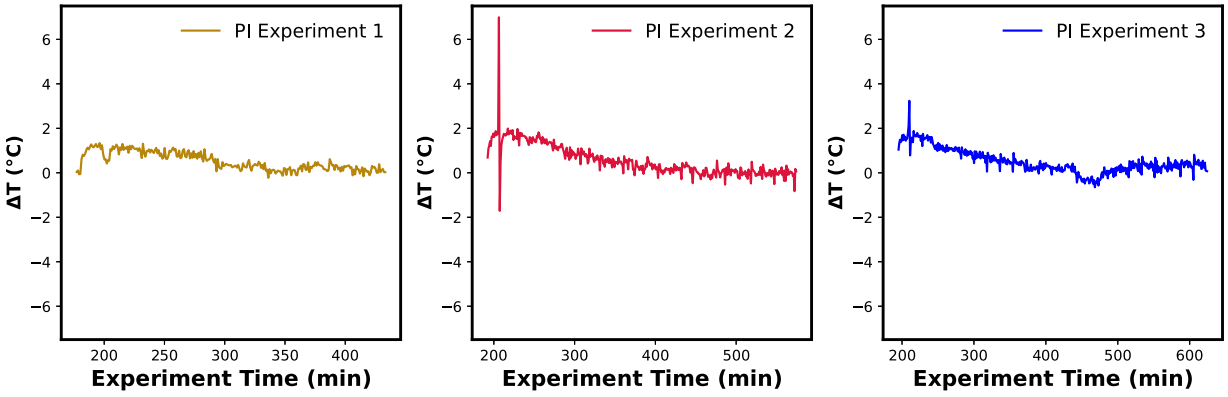

Fig. 20. Change in the reactor outlet temperature over time for all PI experiments.

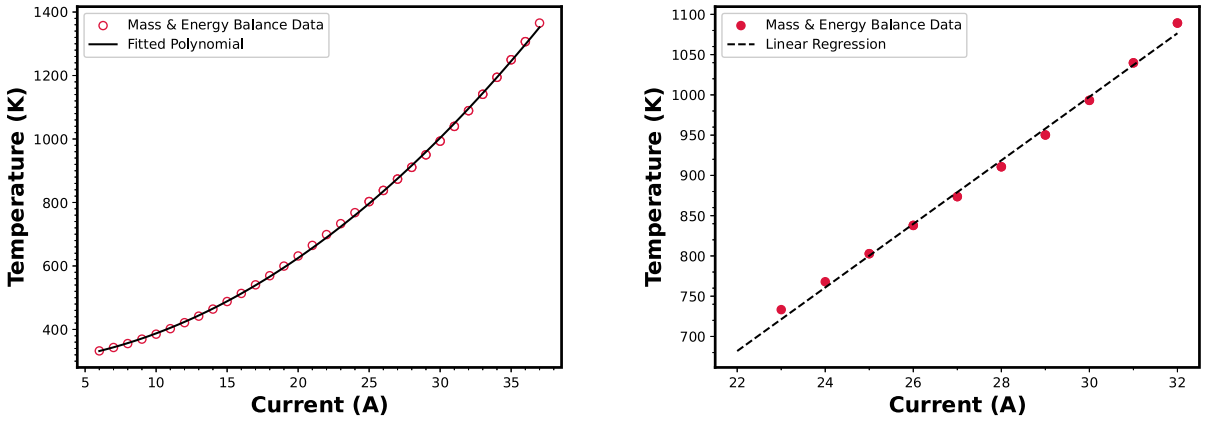

(a) Polynomial fitting of mass and energy balance generated data points.

(b) Linear behavior of current temperature behavior between 700-1100 k.

Fig. 21. Current and temperature relation fitted for MPC current constraints.

$$\text{s.t.} \quad \dot{\bar{x}}(t) = ODE(\bar{x}(t), I(t)),\ \bar{x}(t_k) = \hat{x}(t_k) \tag{18b}$$

$$\bar{F}_{H_2}(t) = h(\bar{x}(t)) \tag{18c}$$

$$L(\bar{x}(t), I(t)) = A(\bar{F}_{H_2}(t) - F_{H_2,sp})^2 + B(I(t) - I_{sp})^2 \tag{18d}$$

$$t \in [t_k, t_{k+2}) \tag{18e}$$

$$|I(t_k) - I(t_{k-1})| \leq 0.013 \tag{18f}$$

$$0\ \text{A} < I < 40\ \text{A} \tag{18g}$$

where the allowed current change is limited to 0.013 A per 5 s, the current range is bounded between 0 and 40 A, $N_h = 2$ is the prediction horizon length, $h(\bar{x}(t))$ is the transformation needed to calculate the hydrogen outlet flow rate from the dynamic model states, the process model is the ODE solver and the optimized cost function is the weighted

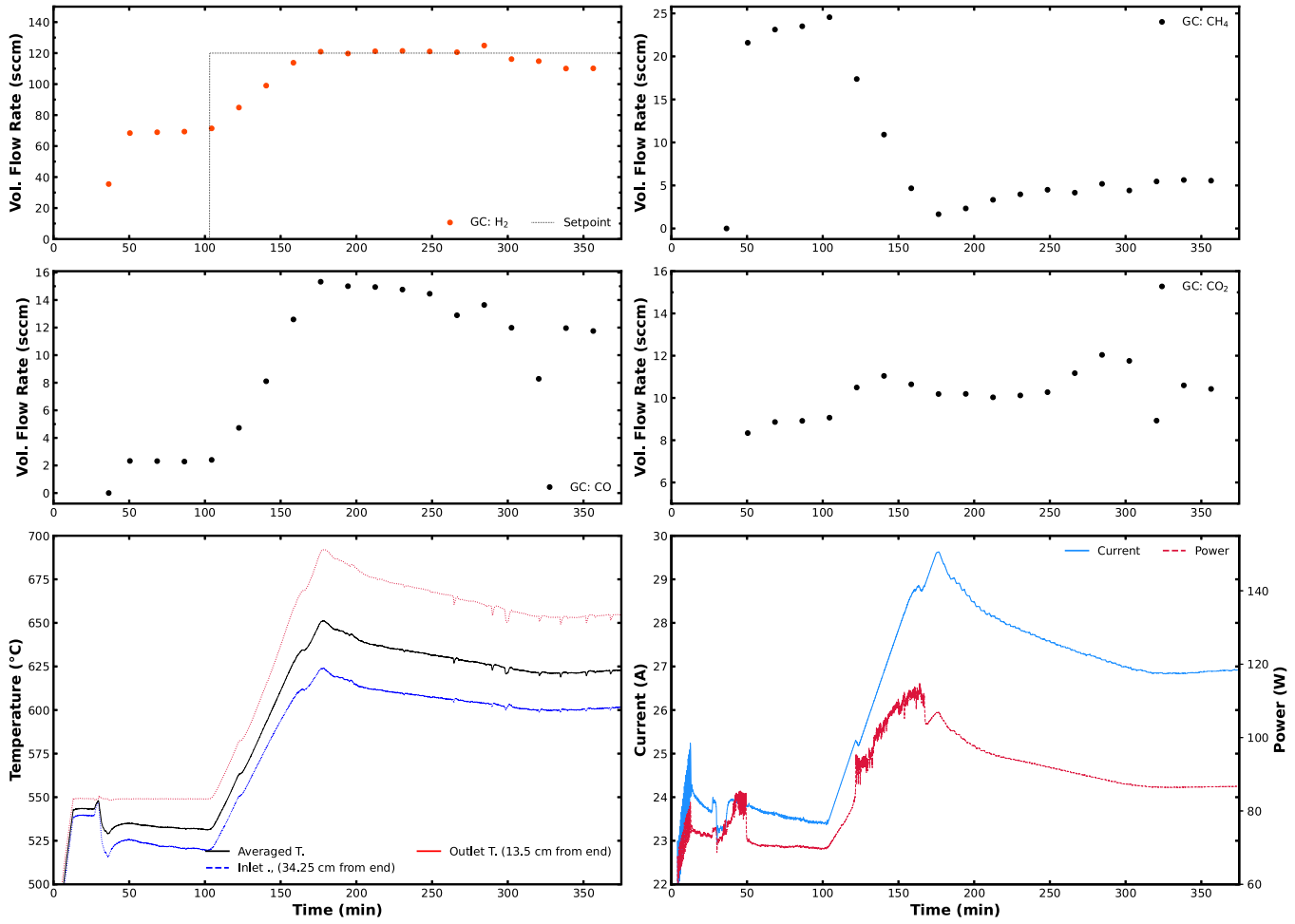

Fig. 22. First closed-loop experiment under MPC.

summation of quadratic errors between the H_2 molar flowrate and the current state estimated by the model, and the current value and the steady-state current estimation at the desired set-point. The A and B values in Eq. (18d) are taken to be 1 and 0.01, respectively. The constraint on the rate of change of the current is imposed so that the temperature in the reactor does not change so fast that the catalyst activity is compromised.

Remark 2. The sensor feedback for other gas outlet flowrates could be incorporated in the ELO to improve the accuracy of the predictions. However, this would require tuning of more parameters in the gain matrix and was not needed in the present experimental implementation due to the achieved closed-loop performance.

6.2.2. Adjustments to experimental conditions

We calculated in the beginning of Section 6.2 that the maximum amount of current increase is 0.013 A from the energy balance equation. However, the experimental setup is vulnerable to phenomena that can cause discrepancies between the model and experimental outputs, such as carbon formation, catalyst deactivation, change in catalyst activity, and delayed heating of insulation layer. Thus, in the experimental setup, the same H_2 production rate can be reached at slightly different temperatures. As a result, if the process control system relies entirely on the model, it may end up not reaching the set-point experimentally even though the model calculates that the process is at steady-state. In order to handle this type of situation, an integral term was added to the MPC output to help the controller drive the process output to the set-point. Considering that the integral term will further increase the MPC output current, the maximum allowed current increment in the MPC formulation was limited to a lesser amount than 0.013. In this case, the current input at each time step was calculated using the following equation:

$$I(\hat{t}) = I_{initial} + \sum_{t=t_0}^{\hat{t}} \Delta I_{MPC} + \frac{1}{\tau_I} \int_{t_0}^{\hat{t}} e(t)\, dt \tag{19}$$

where $\hat{t}$ is the current time step, $I_{initial}$ is the current recorded when the MPC starts, I_{MPC} is the current calculated by the MPC only, and $e(t)$ is the error term between the set-point and the ELO H_2 output. In this case, a τ_I value is selected, and the maximum amount of the current increment provided by the MPC is limited to 0.008 A, which would modify the constraint in Eq. (18f). The integral error term is integrated with respect to the ELO output at each time step. The τ_I value is chosen to be 434 086 s, which is very high, to make sure that the impact of the integral term is small. The main reason for this is that the ELO is tuned such that the H_2 estimation is very close to the previous GC measurement. Hence, until the GC is updated, the H_2 prediction does not increase, causing a significant accumulation of error. Also, it is not desirable for the integral term to take a huge step and violate the current increase constraint. Finally, it is important to point out that an alternative to the addition of an integral term in the MPC control action would be to adopt an offset-free MPC scheme. In the present case, the impact of the integral term is really small (owing to the choice of the gain parameter of this term) and only has an effect as the process output approaches the steady-state; please see the experimental results in the next subsection.

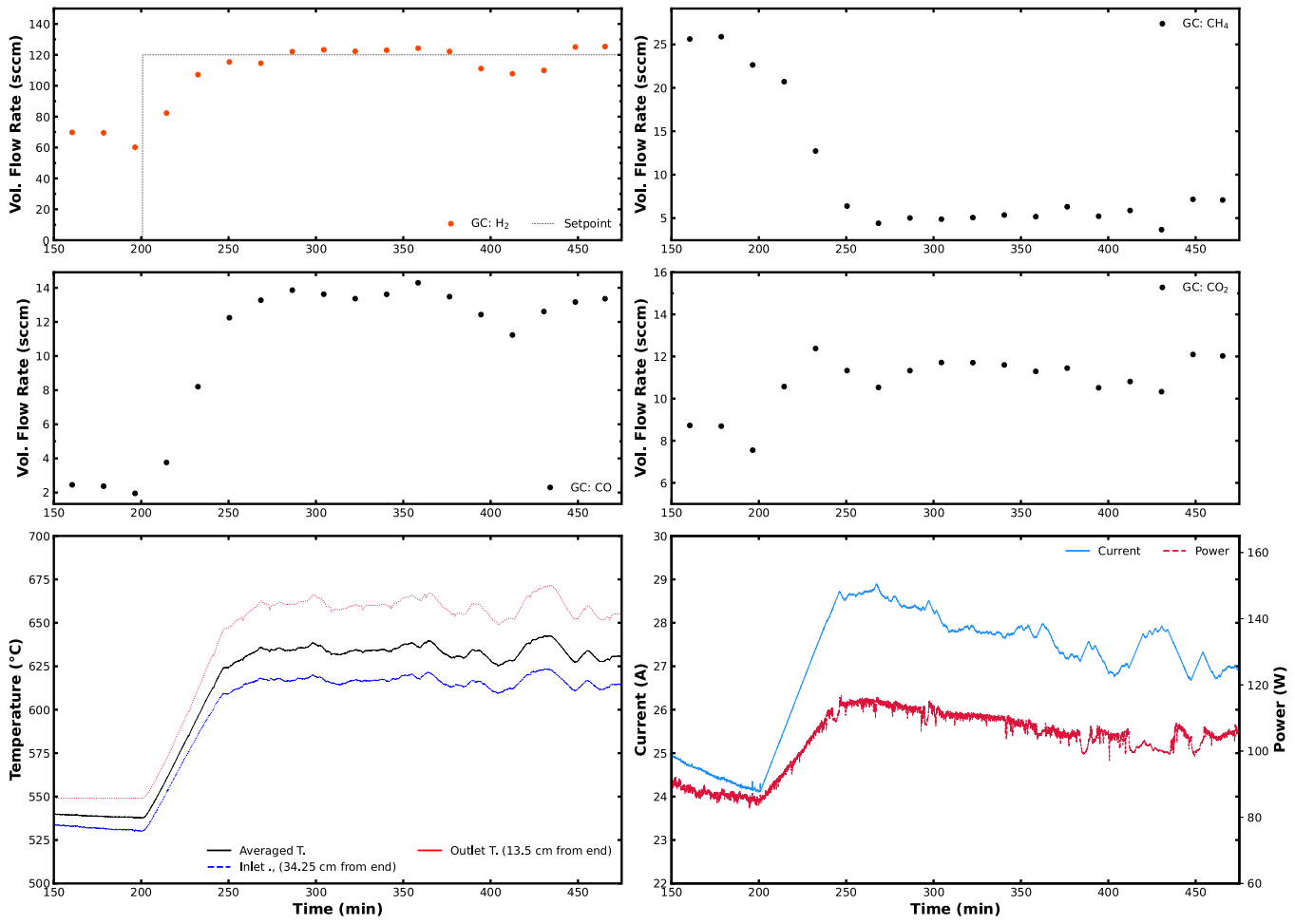

Fig. 23. Second closed-loop experiment under MPC.

In Section 4.2, it was discussed that the insulation layer undergoes a delayed increase in temperature change. This implies that the heat from the reactor wall is conducted through the insulation layer, and then heat is dissipated to the surroundings at 25 °C through convective heat transfer. In the energy balance equation (Eq. (13)), the heat loss is represented with the $UA(T_s - T)$ term, which only accounts for the convection, and is a linear expression. Since the nonlinear conduction heat transfer across the insulation layer is not represented here, it should be represented by a different method for accurate MPC calculations. In order to do that, the heat transfer coefficient times the surface area term in the process model is recalculated every 500 s using the recorded reactor temperature data. This helps to lump convection and conduction into the energy equation and improve MPC predictions. To update the UA term, temperature derivatives are calculated from data history using a centered finite-difference method. Following this, the corresponding temperatures, currents, potentials and ELO predictions are evaluated. These parameters are used to minimize the distance between the experimental heat differential and Eq. (13) to find the most optimal UA term through an SQP (sequential quadratic programming) solver. As the UA term changes, the I_{sp} term in the MPC formulation (Eq. (18d)) that corresponds to the set-point temperature changes as well. Thus, when the UA is recalculated, the procedure mentioned in Section 6.2 is repeated with the new UA value used in the process model to update the current set-point.

Experimental data that the sensors are collecting are very noisy compared to simulation data. For example, the resistance changes often during the experiment, due to oxidation of the current collectors. The temperature signals obtained from the setup are not smooth due to environmental factors and sensor noise. In order to mitigate the effects of the noise, a Savitzky–Golay filter was applied with a polynomial order of 2 and window length of 40 s on current, temperature, and resistance values. Savitzky–Golay filter fits a second order polynomial to the last 40 s of data and uses the fitted polynomial data coefficients to estimate weights for smoothing the data (Savitzky and Golay, 1964). The process model takes data points on a per-second basis, and the noise from the sensors causes noisy predictions. In addition to that, the ELO correction term might cause an amplification of the noise that would be reflected to the output predictions. Thus, de-noising the aforementioned signals will cause less fluctuating predictions in the subsequent gas flowrate estimations.

6.2.3. *Experimental implementation of MPC*

The experimental real-time implementation of the proposed MPC control scheme is conducted with the same initial condition and set-point as the PI control experiments for a fair comparison. We carried out two experiments under MPC using the same operating conditions and MPC tuning parameters. The MPC sampling time is 5 s in the experimental implementation and the MPC was always solved within this time constraint. The first MPC experimental result is presented in Fig. 22 and the second one is presented in Fig. 23. From these two figures, it can be seen that the MPC successfully drives the process to the set-point in both experiments, establishing the reproducibility of

this experimental MPC implementation. Furthermore, it can be seen that it takes around 4 GC measurements for the output to reach the set-point, which corresponds to around 72 min of process operation time, which is a significantly shorter approach to the set-point than all the PI control experiments. Upon regulation at the set-point, the GC results exhibit less variability around the set-point compared to the output under PI control. With respect to the behavior of the control system, the current values calculated by the MPC change smoothly with time, leading to a smooth change of the temperature evolution in the reactor. Finally, we note that the chattering in the power signal is due to the noisy behavior of the voltage and current measurement of the heating system and it is best to view the power consumption in terms of a sufficiently long moving average that would yield the average value over time. We decided to present the instantaneous power consumption in the plots, as it is the primary data, and one can easily determine the average power from these results.

7. Conclusion

Steam methane reforming is a widely used endothermic H_2 production process that can transition to a more sustainable heating provided by electricity. As the amount of academic research focusing on electrified SMR technology development is increasing, the automatic feedback controlled operation of this process has not been adequately explored. Advanced model-based control schemes have not been investigated, mostly due to computational models that take long times to solve in real-time. In this work, we used steady-state experimental data to develop a lumped parameter model for this process that was used in a model predictive control system. During the experimental procedure, the temperature rate of change increase was kept within a 6 °C/min limit to prevent thermal damage to the catalyst. The model was incorporated into an MPC scheme used to drive the SMR process to a new H_2 production set-point. To prove the efficiency of the MPC, PI control experiments were also conducted. While the PI controller successfully drove the H_2 production to the set-point under conditions like catalyst deactivation and coke formation, the MPC was found to be more efficient with a significantly faster approach to the set-point while respecting control action constraints.

CRediT authorship contribution statement

Berkay Çıtmacı: Writing – original draft, Software, Methodology, Investigation, Conceptualization. **Dominic Peters:** Writing – original draft, Methodology, Investigation, Conceptualization. **Xiaodong Cui:** Writing – original draft, Software, Methodology, Investigation, Conceptualization. **Fahim Abdullah:** Writing – original draft, Investigation. **Ahmed Almunaifi:** Investigation. **Parth Chheda:** Investigation. **Carlos G. Morales-Guio:** Writing – review & editing, Writing – original draft, Supervision, Methodology, Investigation, Funding acquisition, Conceptualization. **Panagiotis D. Christofides:** Writing – review & editing, Writing – original draft, Supervision, Methodology, Funding acquisition, Conceptualization.

Declaration of competing interest

The authors declare that they have no known competing financial interests or personal relationships that could have appeared to influence the work reported in this paper.

Acknowledgments

We would like to gratefully acknowledge financial support from the U.S. Department of Energy, United States, through the Office of Energy Efficiency and Renewable Energy (EERE), under the Advanced Manufacturing Office Award Number DE-EE0007613. Financial support from the National Science Foundation, United States is also gratefully acknowledged through the NSF-CBET Award No. 2140506.

References

Almind, M.R., Vendelbo, S.B., Hansen, M.F., Vinum, M.G., Frandsen, C., Mortensen, P.M., Engbæk, J.S., 2020. Improving performance of induction-heated steam methane reforming. Catal. Today 342, 13–20.

Ashik, U., Daud, W.W., Abbas, H.F., 2017. Methane decomposition kinetics and reaction rate over Ni/SiO_2 nanocatalyst produced through co-precipitation cum modified stöber method. Int. J. Hydrog. Energy 42, 938–952.

Çıtmacı, B., Cui, X., Abdullah, F., Richard, D., Peters, D., Wang, Y., Hsu, E., Chheda, P., Morales-Guio, C.G., Christofides, P.D., 2024. Model predictive control of an electrically-heated steam methane reformer. Digit. Chem. Eng. 10, 100138.

Çıtmacı, B., Luo, J., Jang, J.B., Canuso, V., Richard, D., Ren, Y.M., Morales-Guio, C.G., Christofides, P.D., 2022a. Machine learning-based ethylene concentration estimation, real-time optimization and feedback control of an experimental electrochemical reactor. Chem. Eng. Res. Des. 185, 87–107.

Çıtmacı, B., Luo, J., Jang, J.B., Korambath, P., Morales-Guio, C.G., Davis, J.F., Christofides, P.D., 2022b. Digitalization of an experimental electrochemical reactor via the smart manufacturing innovation platform. Digit. Chem. Eng. 5, 100050.

Çıtmacı, B., Luo, J., Jang, J.B., Morales-Guio, C.G., Christofides, P.D., 2023. Machine learning-based ethylene and carbon monoxide estimation, real-time optimization, and multivariable feedback control of an experimental electrochemical reactor. Chem. Eng. Res. Des. 191, 658–681.

Cui, X., Çıtmacı, B., Peters, D., Abdullah, F., Wang, Y., Hsu, E., Chheda, P., Morales-Guio, C.G., Christofides, P.D., 2024. Estimation-based model predictive control of an electrically-heated steam methane reforming process. Digit. Chem. Eng. 11, 100153.

From, T.N., Partoon, B., Rautenbach, M., Østberg, M., Bentien, A., Aasberg-Petersen, K., Mortensen, P.M., 2024. Electrified steam methane reforming of biogas for sustainable syngas manufacturing and next-generation of plant design: A pilot plant study. Chem. Eng. J. 479, 147205.

Ginsburg, J.M., Piña, J., El Solh, T., De Lasa, H.I., 2005. Coke formation over a nickel catalyst under methane dry reforming conditions: Thermodynamic and kinetic models. Ind. Eng. Chem. Res. 44, 4846–4854.

He, L., Fan, Y., Luo, L., Bellettre, J., Yue, J., 2020. Preparation of $Pt/\gamma-Al_2O_3$ catalyst coating in microreactors for catalytic methane combustion. Chem. Eng. J. 380, 122424.

Kalman, R.E., 1960. A new approach to linear filtering and prediction problems.

Luenberger, D.G., 1964. Observing the state of a linear system. IEEE Trans. Mil. Electron. 8, 74–80.

Luo, J., Çıtmacı, B., Jang, J.B., Abdullah, F., Morales-Guio, C.G., Christofides, P.D., 2023. Machine learning-based predictive control using on-line model linearization: Application to an experimental electrochemical reactor. Chem. Eng. Res. Des. 197, 721–737.

Meloni, E., Martino, M., Palma, V., 2020. A short review on Ni based catalysts and related engineering issues for methane steam reforming. Catalysts 10, 352.

Richard, D.M., 2021. Development and Testing of Two Lab-Scale Reactors for Electrified Steam Methane Reforming Master's thesis. University of California, Los Angeles.

Roizard, D., 2016. Antoine equation. In: Encyclopedia of Membranes. Springer Berlin Heidelberg, Berlin, Heidelberg, pp. 97–99.

Savitzky, A., Golay, M.J., 1964. Smoothing and differentiation of data by simplified least squares procedures. Anal. Chem. 36, 1627–1639.

Shomate, C.H., 1954. A method for evaluating and correlating thermodynamic data. J. Phys. Chem. 58, 368–372.

Spagnolo, D., Cornett, L., Chuang, K., 1992. Direct electro-steam reforming: A novel catalytic approach. Int. J. Hydrog. Energy 17, 839–846.

Ting, T.L., Hasanah, N.W., Rohman, F.S., Muhammad, D., 2023. Modeling and control of steam methane reforming process using model predictive control. ASEAN J. Process Control 2, 1–13.

Wismann, S.T., Engbæk, J.S., Vendelbo, S.B., Bendixen, F.B., Eriksen, W.L., Aasberg-Petersen, K., Frandsen, C., Chorkendorff, I., Mortensen, P.M., 2019. Electrified methane reforming: A compact approach to greener industrial hydrogen production. Science 364, 756–759.

Wismann, S.T., Engbaek, J.S., Vendelbo, S.B., Eriksen, W.L., Frandsen, C., Mortensen, P.M., Chorkendorff, I., 2021. Electrified methane reforming: Elucidating transient phenomena. Chem. Eng. J. 425, 131509.

Wu, Z., Aguirre, A., Tran, A., Durand, H., Ni, D., Christofides, P.D., 2017. Model predictive control of a steam methane reforming reactor described by a computational fluid dynamics model. Ind. Eng. Chem. Res. 56, 6002–6011.

Xu, J., Froment, G.F., 1989. Methane steam reforming, methanation and water-gas shift: I. intrinsic kinetics. AIChE J. 35, 88–96.

Zhang, H., Sun, Z., Hu, Y.H., 2021. Steam reforming of methane: Current states of catalyst design and process upgrading. Renew. Sustain. Energy Rev. 149, 111330.

Zheng, L., Ambrosetti, M., Zaio, F., Beretta, A., Groppi, G., Tronconi, E., 2023. Direct electrification of Rh/Al_2O_3 washcoated SiSiC foams for methane steam reforming: An experimental and modelling study. Int. J. Hydrog. Energy 48, 14681–14696.